Li Tao (Orcid ID: 0000-0002-3563-8245)

Chen Jie (Orcid ID: 0000-0002-3618-2032)

Thompson Jobe Jessica A (Orcid ID: 0000-0001-5574-4523)

Burbank Douglas (Orcid ID: 0000-0001-8497-3296)

Li Gang Zhi (Orcid ID: 0000-0003-0394-9345)

He Xiaohui (Orcid ID: 0000-0001-8609-4105)

Zheng Wenjun (Orcid ID: 0000-0002-0357-9279)

Zhang Peizhen (Orcid ID: 0000-0002-5656-8442)

Along-Strike and Downdip Segmentation of the Pamir Frontal Thrust and its Association with the 1985 M_w 6.9 Wuqia Earthquake

Tao Li[1, 2], Zhuxin Chen[3], Jie Chen[1], Jessica A. Thompson Jobe[4, #], Douglas W. Burbank[5], Zhigang Li[2], Xiaohui He[2], Wenjun Zheng[2], Peizhen Zhang[2], Boxuan Zhang[2]

[1]State Key Laboratory of Earthquake Dynamics, Institute of Geology, China Earthquake Administration, Beijing, China

[2]Guangdong Provincial Key Lab of Geodynamics and Geohazards, School of Earth Sciences and Engineering, Sun Yat-sen University, Guangzhou, China

[3]Research Institute of Petroleum Exploration and Development, PetroChina, Beijing, China

[4]Institute of Tectonic Studies, Department of Geological Sciences, The University of Texas El Paso, El Paso, TX, USA

[5]Department of Earth Science, University of California Santa Barbara, Santa Barbara, CA, USA

[#]Now at Geologic Hazards Science Center, United States Geological Survey, Golden, CO, USA

Abstract

The Pamir Frontal Thrust (PFT) along the leading edge of the northern Pamir is characterized by multiple earthquakes with moment magnitudes of 6.5-7.1. Geometric characteristics of the PFT corresponding to these earthquakes and to future seismic hazards, however, remain largely unexplored. This study focuses on the easternmost segment of the PFT, where the M_w 6.9 Wuqia earthquake occurred in 1985. Through interpretation of available 2D seismic reflection profiles and surface mapping data, we develop a 3D geometric model for the fault plane. Our results illustrate that, at depth, the fault plane is separated by a sub-horizontal detachment horizon into upper and lower ramps, and both ramps are significantly segmented, along strike, by transfer faults or lateral ramps as well. Such along-strike and downdip segmentation of the thrust sheet apparently plays a significant control on seismic rupture process of the Wuqia earthquake and can well explain why the region is characterized by moderate-magnitude (M_w 6.5-7.1) events. Additionally, our study helps quantify key constraints on the Cenozoic deformation and evolution of the northeastern Pamir and, specifically, determines a total shortening of ≤43 km at the Pamir front: accommodating about 15% of the total indentation of the Pamir range into Central Asia.

Key Points:

(i) The PFT fault plane is significantly segmented both in the downdip direction and along strike

(ii) Rupture of the 1985 Wuqia earthquake is likely encompassed within the upper ramp of the Tuomuluoan PFT fault segment

(iii) Total shortening at the Pamir front is ≤43 km: significantly less than ~300-km-northward Cenozoic indentation of the Pamir

1. Introduction

Active faults commonly include multiple segments along strike that are separated by stepovers, high-angle fault bends, or transfer faults (e.g., Davis et al., 2012; Yeats et al., 1997). These discontinuities can stop rupture propagation and, hence, limit the rupture length during an earthquake. Despite several exceptions (e.g., the complex fault system triggering the 2016 Kaikōura earthquake in New Zealand; Hamling et al., 2017), a 4-5 km stepover or an ~20° fault bend for strike-slip faults and a 5-7 km stepover for normal faults can generally act as an effective barrier for seismic rupture propagation, as documented by abundant coseismic surface-break traces (e.g., King & Nabelek, 1985; Wesnousky, 2006, 2008; Zhang et al., 1999) and numerical modeling (e.g., Harris & Day, 1993; Lozos et al., 2011). Along-strike discontinuities or segmentation, therefore, have proven to be quite useful to prospectively estimate potential maximum earthquake magnitudes and evaluate associated seismic hazards for strike-slip and normal faults (e.g., DuRoss et al., 2016; Schwartz & Coppersmith, 1984; Wesnousky, 2006).

Comparatively, the potential seismic rupture length and magnitude of thrust faults in contractional orogenic forelands appear to be more unpredictable. On the one hand, each along-strike segment may represent a single seismic source, as exemplified by the 1983 M_w 6.5 Coalinga event in central California, USA and the 2015 M_w 6.4 Pishan event at the Western Kunlun piedmont, China (Guzofski et al., 2007; T. Li et al., 2016). On the other hand, these thrust faults typically dip gently and extend downward far away from their surface traces and merge with horizontal or subhorizontal detachment horizons that then join a lower ramp rooting beneath the uplifted terrain (Figure 1; e.g., Avouac, 2015; Avouac et al., 1993; Guilbaud et al., 2017; Hubbard et al., 2010, 2016; T. Li et al., 2018; Yue et al., 2005). Consequently, the cross-section geometry of a thrust fault commonly has a wide low-angle fault plane at depth and can include multiple fault ramps and flats defined by fault bends. Such downdip linkage and segmentation can exert an essential control on the seismic rupture as well. For example, during the 1505 M_w 8.2 Lo Mustang event and the 1934 M_w 8.2 Bihar-Nepal event along the Himalaya front, and the 1906 Manas event (M_w 7.4-8.2) along the northern Tian Shan front, China, the lower ramp is proposed to have ruptured simultaneously with a detachment horizon and an upper ramp (e.g., Avouac, 2015; Rajendran et al., 2017; Stockmeyer et al., 2014). Nonetheless, the recent 2015 M_w 7.8 Gorkha event near the Himalaya front only ruptured the up-dip, gently-dipping detachment that is bounded by steeply-dipping ramps at its top and bottom (Hubbard et al., 2016). Additionally, during the 2013 M_w 6.6 Lushan event at the eastern Tibet front, only the lower ramp of the thrust sheet was ruptured (Y. Li et al., 2014; M. Wang et al., 2014).

Because the seismic rupture process can be limited by both along-strike and downdip segmentation of the fault plane, it is expected that each segment of the lower ramp, upper ramp, and even the detachment can act as a single, independent seismic source if the lower and upper ramps are significantly segmented along strike by lateral ramps and are separated by a broad detachment horizon at depth (Figure 1a). Otherwise, if the lower and upper ramps are sufficiently unsegmented along strike and the detachment horizon is relatively narrow, an earthquake sourced on the lower ramp can release enough seismic moment to rupture all of the lower ramp, as well as the detachment and upper ramp (Figure 1b). To accurately evaluate potential seismic hazards of this type of active thrusts, therefore, adequate constraints on the 3D fault-plane geometry are essential.

Lying at the northwestern indentation corner of the Indo-Asian collision system, the arcuate Pamir is characterized by notably strong intracontinental seismic activity in a global context (Figure 2 inset). Along the Pamir Frontal Thrust (PFT) near its northern expression, multiple earthquakes with moment magnitudes of 6.5-7.1 have been recorded during the historical and instrumental period, but no larger earthquakes (Figure 2). This behavior apparently contrasts with the foreland thrust system, for example, at the Himalaya and Tian Shan fronts, where earthquakes with M_w ≥7.5 and even M_w ≥8.0 have been recorded (e.g., Mugnier et al., 2013; Molnar & Deng, 1984). This contrast in rupture behavior raises questions about the geometric characteristics of the PFT that are responsible for these recorded M_w 6.5-7.1 events. Is there evidence for geometric segmentation that limits the extent of ruptures? Does the PFT have the potential to generate larger, more devastating earthquakes? These questions remain unanswered at present, partially because knowledge of the PFT's subsurface geometry is very limited.

This study focuses on the 1985 M_w 6.9 Wuqia earthquake at the easternmost segment of the PFT (Figures 2 & 3), an area where a dense grid of petroleum industry 2D seismic reflection profiles provides a unique opportunity to tightly constrain the 3D fault-plane geometry of the PFT (see Figure S1 for locations of these profiles). Through detailed interpretations of these profiles and surface mapping data, we describe key insights into (i) the geometric characteristics of the PFT and their association with the Wuqia and other M_w 6.5-7.1 events and (ii) the potential seismic hazards of the PFT. Our study suggests that the significant along-strike and downdip segmentation of the PFT helps explain the 20th-century M_w 6.5-7.1 events, as well as future seismic hazards.

We first present the geologic setting to illuminate the study area's stratigraphy, major structures, and previous tectonic deformation (sections 2 and 3); followed by our interpretative methods and results, including structural cross sections and 3D fault-plane geometries derived in part from seismic reflection profiles (sections 4, 5 and 6); and seismic parameters of the Wuqia and other major events that have occurred on the PFT (section 7).

On these bases, we determine the rupture patch of the Wuqia event and draw some speculative conclusions that could have implications for regional seismic hazards (sections 8.1 and 8.2). Our new structural model based on detailed subsurface mapping also places constraints on the Cenozoic deformation and evolution of the northern Pamir (section 8.3).

2. Tectonic Setting

The Pamir orogen comprises amalgamated continental fragments that were successively sutured with southern Asia during the Paleozoic and Mesozoic (Burtman & Molnar, 1993, and references therein). In the course of the Cenozoic India-Asia collision, the Pamir has indented northward ~300 km relative to stable Asia (Blayney et al., 2016; Burtman & Molnar, 1993; Cowgill, 2010; Schwab et al., 2004). This indentation is accommodated by the sinistral Darvaz Fault on the western margin, the dextral Kashgar-Yecheng Transfer System on the eastern margin, as well as by thrust faulting and crustal shortening in the interior and surrounding area of the Pamir (Burtman & Molnar, 1993; Chapman et al., 2017; Coutand et al., 2002; Cowgill, 2010; Sobel et al., 2011). Beneath the Pamir, the indentation drives Asian lithosphere (including mantle and lower crust) to descend as deep as ~250 km to form a steeply south-dipping subducting slab (e.g., Schneider et al., 2013; Sippl et al., 2013).

The northern flank of the Pamir is delineated by the Pamir foreland thrust system, which is dominated by the Main Pamir Thrust (MPT) and the PFT (Figure 2). The thrust system accommodates a shortening rate of 10-15 mm/a according to GPS geodesy, and it localizes most of the modern convergence between the Pamir and central Asia (Yang et al., 2008; Zubovich et al., 2010, 2016). The MPT, the boundary fault of the Pamir range and its foreland basin, initiated in the late Oligocene-early Miocene (Cao et al., 2013; Sobel &

Dumitru, 1997; Sobel et al., 2013). Its Quaternary slip rate, however, appears to be quite low (<1 mm/a), such that the regional convergence is now concentrated on the PFT, lying tens of kilometers north of the MPT (Arrowsmith & Strecker, 1999; Bufe et al., 2017; T. Li et al., 2012, 2013; Thompson Jobe et al., 2017; Zubovich et al., 2010). The PFT initiated approximately 5-6 Ma, representing the latest, major forelandward propagation of the Pamir (Thompson et al., 2015). From west to east (Figure 2), the fault is characterized by one or two splays in the Alai Valley, widens and branches into more splays at the eastern end of the Alai Valley, then connects with the primarily top-to-NE thrusts and folds at the western end of the Tarim Basin. Detailed mapping of its surface trace indicates that the fault can be subdivided into multiple segments connected by transpressional transfer faults (Figures 2 & 3; Arrowsmith & Strecker, 1999; T. Li et al., 2012, 2013; Thompson Jobe et al., 2017). The PFT exhibits a high level of seismicity (e.g., Fan et al., 1994; Schurr et al., 2014): frequent earthquakes with moment magnitudes of ≥5.0 have been recorded along the fault, including the 1974 M_w 7.1 Markansu, 1978 M_w 6.6 Zaalay, 1985 M_w 6.9 Wuqia, and 2008 M_w 6.6 Nura events (Figure 2; Table 1).

To the north of the Pamir, the narrow intermontane Alai Valley is the remnant of the formerly contiguous Tajik-Alai-Tarim basin. During northward indentation and uplift of the Pamir, the basin was overridden and subsided significantly, and is now filled by up to 8 km of continental clastic sediments following late-Cretaceous and Paleogene marine deposition (Coutand et al., 2002; Jia et al., 2004). Farther north, the southern Tian Shan began to uplift at 18-25 Ma and subsequently propagated southward to produce a foreland thrust system as well (Allen et al., 1999; Heermance et al., 2008; Sobel et al., 2006; Thompson Jobe et al., 2018; X. Wang et al., 2011; Yin et al., 1998).

3. Overview of the Surface Geology

The 1985 Wuqia earthquake occurred at the northeastern margin of the Pamir (Figures 2 & 3), where the north-vergent Pamir foreland thrust system and the south-vergent southern Tian Shan foreland thrust system begin to interfere with each other and expose Proterozoic through Pleistocene strata.

3.1. Stratigraphy

Proterozoic rocks, constituting the basement of the Tarim Basin, are dominated by low grade metasediments (Jia et al., 2004). These rocks crop out in the southern Tian Shan and at the core of the Wulagen anticline (Figure 3b). Representing cycles of marine transgressions and regressions (Jia et al., 2004), the overlying Paleozoic strata consist of shallow marine carbonates and neritic marine carbonates interbedded with shale, mudstone, and sandstone. Regionally, these strata significantly vary in thickness: >5000 m thick within the Pamir and southern Tian Shan, but not preserved at the Wulagen anticline (marked WLG in Figure 3). Both Proterozoic and Paleozoic strata are intensely deformed from tectonic events predating Cenozoic deformation and are unconformably overlain by a Mesozoic-Cenozoic sedimentary sequence (Figure 4; Jia et al., 2004).

The Mesozoic strata include Upper Triassic sandstone and conglomerate (Jia et al., 2004), Jurassic coal-bearing mudstone, sandstone and conglomerate (thickness ranging from >4000 m to 0 m) (Jia et al., 2004; Sobel, 1999), and Lower Cretaceous terrestrial sediments (~1000 m) that were succeeded by Upper Cretaceous marine sediments (300-400 m) deposited during transgressions of the Tethys sea (Figure 4; Bershaw et al., 2012; Liu et al., 2016). Besides local exposures at the Pamir front, the Mesozoic strata are observed predominantly on the margins of the southern Tian Shan (Figure 3b).

Cenozoic strata, characterized by a coarsening-upward sequence that lie conformably or subparallel unconformably above the Upper Cretaceous strata, are exposed widely in the basin area (Figures 3b & 4). Their thickness remains relatively stable across the basin (5000- to 8000-m-thick): a notable contrast with the striking thickness variations of the Paleozoic and Mesozoic strata.

The Paleogene Kashi Group is 900-1700 m thick and records several alternations of shallow marine, hypersaline lagoon, and fluvial deposits (Figure 4; e.g., Bershaw et al., 2012; Liu et al., 2016; Sun & Jiang, 2013). At the Biertuokuoyi section and in the borehole Wupar #1, these strata are characterized by massive gypsum, gray-green fossiliferous limestone, and red, purple mudstone and siltstone (Figure 4). At the Oytagh section, however, the lithology is characterized by conglomerates, siltstone, muddy gypsum, and limestone. Hence, facies variations are notable across a <100-km distance. As identified in previous studies (e.g., H. Chen et al., 2010; Cheng et al., 2016), the Paleogene strata constitute the most important detachment horizon in the region.

Conformably overlying the Paleogene strata, the Miocene Wuqia Group consists of gray-green medium- to coarse-grained sandstone and conglomerate interbedded with red-brown mudstone and siltstone, implying a typical terrestrial depositional setting (Figure 4). The strata are ~2000 m thick at Oytagh and increase to 3000-4000 m at Wupar #1 and Biertuokuoyi. These wedge-shaped deposits are interpreted to be formed synchronously with uplift of the Pamir and southern Tian Shan.

The Pliocene Atushi Formation conformably overlies the Miocene strata and comprises gray-yellow to tan sandstone, siltstone, mudstone, and rare pebble conglomerate (Heermance et al., 2007; Jia et al., 2004). These strata have a thickness ranging from ~4000 m at the Atushi anticline (Heermance et al., 2007) to 0 m to the south of the PFT (Figure 3b).

The Xiyu conglomerate, crosscutting the Miocene and Pliocene strata along angular or subparallel unconformities, represents significantly time-transgressive gravel deposits sourced from uplifted mountain areas (Figure 3b; Heermance et al., 2007; Jia et al., 2004; Thompson Jobe et al., 2018).To the north of the PFT, the strata are characterized by remarkable, gray blocky conglomerate with ages varying from the middle-Miocene to Pleistocene (Heermance et al., 2007).In contrast, south of the PFT, the strata are dominated by gray conglomerate containing sandstone layers with a basal age of approximately 5-6 Ma (Figure 4), constrained by a combination of magnetostratigraphy and burial cosmogenic dating (Thompson et al., 2015; Thompson Jobe et al., 2018). These strata are interpreted to be syntectonic or piggy-back basin deposits associated with the PFT (Thompson et al., 2015).

3.2. Surface Structures

On the surface, the Pamir thrust system includes three subparallel thrust faults (Figure 3): the Pamir Frontal Thrust (PFT) along its leading edge, the Main Pamir Thrust (MPT) bounding the Pamir range, and the Takegai Thrust between these two faults.

The PFT, locally called the Wupaer Thrust (e.g., Cheng et al., 2016; Wei et al., 2013) or Kazkeaerte Fault (e.g., J. Chen et al., 1997), is characterized by an array of ESE-trending, right-stepping thrusts and folds (Kabajiate, Tuomuluoan, Aismaola, and Mushi) that are connected by SE- to S-trending transfer faults with motion of dextral oblique thrusting (Figure 3). The PFT raises and exposes the entire Cenozoic sedimentary sequence in its hanging wall, among which the Paleogene and Miocene strata are intensely deformed into numerous mesoscale folds. Along the fault trace, a series of outcrops reveal that Paleogene strata, comprising the regional detachment horizon, override Neogene or Quaternary deposits along a hanging-wall bedding-parallel fault plane (Figure 5). The fault branches into three to five splays farther west, whereas it merges with the MPT at the mountain front farther east (Figure 3).

The MPT is recognized by the contact between Paleozoic and Mesozoic-Cenozoic sequences (Figure 3). The fault is well exposed in its western portion but is mostly buried beneath Quaternary piedmont alluvium in its eastern portion. Although the MPT delimits a striking topographic contrast at its north and south sides and is commonly regarded as the principal fault of the Pamir thrust system (e.g., Burtman and Molnar, 1993; Coutand et al., 2002; Sobel and Dumitru, 1997), field mapping and seismic profile interpretations suggest that its total slip amount is quite limited (H. Chen et al., 2010; Cheng et al., 2016). The topographic contrast, therefore, more likely results from differential uplift above a deeply buried thrust ramp below the MPT and differential erosion due to lithologies with contrasting rock strength. Along the fault trace, deformed Plio-Pleistocene Xiyu conglomerate and clearly raised middle-late Pleistocene alluvial fans indicate its Pleistocene activity (Thompson Jobe et al., 2018). During recent times (perhaps Holocene), however, the MPT’s activity has been interpreted to have significantly slowed or ceased, as evidenced by the absence of clearly offset geomorphic surfaces (T. Li et al., 2012; Thompson Jobe et al., 2017).

The Takegai Thrust lies in the Biertuokuoyi piggyback-basin between the MPT and PFT (Figure 3). Slip along this fault causes overthrusting of Miocene sandstone and mudstone above Plio-Pleistocene conglomerate. Where observed at the Biertuokuoyi water gap, the Miocene strata in the hanging wall are highly deformed into mesoscale folds and faults, and the overlying Plio-Pleistocene Xiyu conglomerate drapes over the tip of the Takegai Thrust and merges with the coeval conglomerate in the footwall (Thompson et al., 2015).

4. Methodology

Structural cross sections of the Pamir thrust system have been interpreted in previous studies (e.g., H. Chen et al., 2010; J. Chen & He, 2018; Cheng et al., 2016; Wei et al., 2013). Nonetheless, most cross sections are unbalanced, and each section is fundamentally different from each other due to complicated structural deformation, significant thickness variations of the Paleozoic-Mesozoic units, and the limited length and poor quality of seismic reflection profiles. Building on these existing interpretation results, in this study, we strive to develop improved structural cross sections by: (i) analyzing more and higher-quality seismic profiles, (ii) conducting detailed geologic and structural mapping, (iii) using available low-temperature thermochronologic data, which can constrain the maximum fault-throw magnitude of the thrust system, and (iv) assessing balanced cross sections.

4.1. Interpretations of Seismic Reflection Profiles

We examined a total of 35 seismic reflection profiles (including 23 NE- to N-trending and 12 NW- to W-trending lines) that were collected in 1995-2005 by PetroChina Company (see Figure S1 in supporting information for locations). Seven profiles are interpreted in detail with the goal of developing structural cross sections that characterize the deformation style and evolution of the Pamir thrust system. Other profiles are used to constrain the 3D subsurface geometry of the PFT.

Seismic velocities for the local stratigraphy are unknown. Given the velocity of 3000-5000 m/s of the Paleozoic-Cenozoic strata at the Atushi-Kashi fold belt immediately north of the PFT (Figure 3; Heermance et al., 2008), we assume a uniform velocity of ~4000 m/s as a first-approximation velocity model to conduct time-depth conversions. Because the shallow upper-Cenozoic strata have a typical velocity of <4000 m/s, whereas the deep, consolidated Paleozoic strata have a typical velocity of >4000 m/s, the assumption of a uniform velocity of ~4000 m/s will somewhat increase the dip and depth of fault planes within the upper-Cenozoic strata, but will decrease the dip and depth of fault planes within the Paleozoic strata. The associated dip and depth changes are expected to be less than ±6° and ±3 km, respectively, given the commonly low dip (<30°) of fault planes.

On cross sections, six (or seven) stratigraphic units, including Proterozoic, Paleozoic, Mesozoic, Paleogene, Neogene, and Pliocene-Quaternary (or Pliocene and Quaternary) units are determined through correlations with well-log data of borehole Wupar #1 and stratal outcrops (Figures 3 and 4). The geometry of major faults within the basin can be interpreted using direct fault-plane reflection, truncation of seismic reflections, and downward terminating hinge zones. Deep ramps of the PFT lying beneath the Pamir, however, cannot be interpreted straightforwardly because they are not seismically resolved. We use the Mesozoic-Cenozoic bed geometry in the hanging wall to extrapolate their locations and dips following fault-bend fold theory (Shaw et al., 2005; Suppe, 1983). In the interpretation process, bed dips at the surface (not including dips of Paleozoic strata because they were strongly deformed prior to Cenozoic deformation; Allen et al., 1993; Windley et al., 1990) from geologic maps and our field measurements are synthesized. Such surface data are also used to constrain geometries of the Wulagen, Mingyaole, Mushi, and Oytagh folds, which are not imaged on seismic profiles.

With constraints of subsurface and surface geology, we develop cross sections of the Pamir thrust system that are additionally based on assumptions that: (i) basic geometric elements (e.g., the number of faults and the geometry of fault surfaces) remain similar or change gradually along the strike of the thrust system, and (ii) the total slip amount decreases from west to east due to the eastward decreasing hanging-wall exhumation (Sobel et al., 2013).

Shortening estimates are primarily based on line-length balancing, assuming that the bed does not change from its original length during folding and faulting process. For the Mushi fold experiencing significant pure shear strain (T. Li et al., 2013), the shortening is determined via the excess-area method after Epard & Groshong (1993), assuming that area is conserved within the cross section. Forward modeling in 2D MOVE is used to help to develop balanced cross sections.

4.2. Fault-Throw Magnitude Constrained by Thermochronologic Samples

Low-temperature thermochronologic data can delimit the timing and magnitude of hanging-wall exhumation concurrent with fault displacement (e.g., Heermance et al., 2008; Lease et al., 2012; Reiners & Brandon, 2006; Sobel et al., 2013). In this study, we use available thermochronologic data as another constraint in cross-section development. As illustrated in Figure 6, the fault-throw magnitude (*U*) of the hanging wall relative to the footwall can be calculated by:

$$U = \mathit{Exhumation\ (hanging\ wall) + Net\ Surface\ Uplift\ (hanging\ wall) + Subsidence\ (footwall)}$$

Close to the southern part of the profile *C* (Figure 3b), samples 99WT-39 and 99WT-43 (taken from Paleozoic rocks) yield apatite-fission track (AFT) ages of 74.0±15.0 and 61.0±12.0 Ma, respectively (Sobel et al., 2013). Both samples are interpreted as partially reset, indicating that Cenozoic burial reheating of the Paleozoic strata exposed on the surface today did not exceed ~130°C, the nominal closure temperature of AFT dating (Reiners & Brandon, 2006). Assuming a geothermal gradient of 25°C/km and ~5°C mean annual surface temperature (Sobel & Dumitru, 1997; Sobel et al., 2013), <5 km strata overlying the samples were exhumed during the Cenozoic.

We select the Paleogene strata (Kashi Group) as a reference marker to calculate the hanging-wall net surface uplift and the footwall subsidence, because (i) the unit can be traced continuously across the basin (Figure 4); (ii) the Paleogene unit was deposited before tectonic deformation at the Pamir front, such that it records the total Cenozoic deformation magnitude of the Pamir thrust system, and most importantly, (iii) the upper boundary of this unit was deposited during a transition from marine to continental conditions; thus, its original elevation should be close to Paleogene sea level and nearly horizontal.

In the hanging wall, no Paleogene strata are preserved in the Pamir interior (Figure 3b). If the Paleogene strata had been previously deposited (Figure 6a), their original surface elevation should have been close to the sea level, such that the modern elevation of ~3 km (elevation of thermochronologic samples) can approximate the post-Paleogene net surface uplift. Alternatively, if the original surface of the hanging-wall strata was above the sea level, the net surface uplift would be <3 km (Figure 6b). In the PFT footwall, Paleogene strata lie presently ~4 km below sea level (Figures 7-9), representing an equivalent amount of subsidence. Note that our calculations ignore the influence of stratal compaction and global sea-level change during the Cenozoic. Overall, based on the described sample locations, the fault-throw magnitude of the hanging wall is <12 km relative to the footwall: <5 km of the hanging-wall exhumation based on thermochronology, <3 km net surface uplift from post-Paleogene hanging-wall uplift, and <4 km post-Paleogene footwall subsidence. When combined with the fault dip determined from seismic interpretations, the maximum fault slip can be calculated.

5. Structural Cross Sections of the Pamir Foreland Thrust System

5.1. Basic Observations and Interpretations

Along the Kabajiate-Tuomuluoan fault segments (KaT and TT: Figures 7 & 8 inset), the most prominent structure observed on seismic images is the south-dipping PFT upper ramp that separates strongly deformed strata to the south from gently deformed or even horizontal strata to the north (Figures 7 & 8). The ramp dips downward from the land surface, generally parallel to the Cenozoic strata in its hanging wall. Subsequently, it cuts through the Paleozoic-Mesozoic strata, then, at depths of 9-12 km, flattens to a detachment horizon (basal detachment) across a synclinal fault bend, whose location is marked by the termination of the hinge Z_1 in the hanging wall. The lithology of this detachment is unknown. One possibility is the Middle-Upper Devonian unit: the lowest Paleozoic strata exposed in the region. As described by Jia et al. (2004), its lithology is dominated by interbedded limestone, shale, and mudstone, and it may act as a regional detachment. The other possibility is the gypsiferous mudstone and muddy limestone of the Cambrian strata, which is the main detachment horizon of the Kepintagh fold belt of the southern Tian Shan (e.g., Allen et al., 1999; Yin et al., 1998), ~200 km northeast of our study area (Figure 2 inset). These strata may extend into the study area, but are not exposed on the surface. To the south, uplifted strata at the mountain front indicate that the PFT flat along the detachment subsequently cuts down the section along its lower ramp.

Above the basal detachment, imbricated thrust ramps F1 and F2 can be identified by direct fault-plane reflections and terminations of kink bands (Figures 7 & 8; Figures S2-S4 in supporting information), whereas the thrust ramp F3 is speculated in order to match with

Mesozoic-Cenozoic bed dips on the surface. These faults stack together and sole upward into a detachment horizon (upper detachment) localized along Paleogene gypsum and muddy limestone, which is clearly imaged by strong, continuous seismic reflections. The hanging wall bed geometry matches a solution of original flat-ramp style of these faults: the flat is localized in the upper detachment, and the lower ramp dips deep down beneath the Pamir. The upper detachment ultimately connects to the PFT upper ramp at 5-7 km depth (Figures 7 & 8). Because the fault at higher structural levels is passively transported and refolded due to slip on the lower fault, these ramp-flat thrusts are interpreted to be formed in a forward-breaking sequence.

The Paleozoic-Mesozoic strata thin gradually to the east and pinch out at the Aismaola segment (marked AT: Figure 9 inset), such that the lower detachment merges onto the upper detachment at 6-8 km depth (Figure 9a). This detachment connects with the bedding-parallel PFT upper ramp to the north and four imbricated ramps (PFT lower ramp, F1, F2, and F3) occurring in the Proterozoic strata to the south.

In the Cenozoic sequence, all seismic profiles image an abrupt regional angular unconformity that marks the contact between the Miocene and the Pliocene-Quaternary deposits (Figures 7-9). Below the unconformity, the Paleogene-Miocene strata are manifested by chaotic seismic reflections interpreted to be strongly deformed by localized faulting and associated folding. Preserved structures in these strata are challenging to interpret, with the exception of several faults that can be identified by their direct seismic reflections. Comparatively, the overlying Pliocene-Quaternary sequence is characterized by well-defined and continuous reflections. The strata occupy the Biertuokuoyi piggyback basin and progressively overlap the older strata at the Pamir front and the PFT hanging wall. On profiles *C-E* (Figures 7 & 9a), strata are deformed predominantly in a gentle, broad syncline, with local and weak fault disruptions of the basal strata. On profiles *A* and *B* (Figure 8), however, the Takegai Thrust moderately deforms the Pliocene-Quaternary strata and divides the unified syncline into two synclines. These observations indicate that a significant transition in the regional deformation occurred in the late Miocene-early Pliocene (around 5-6 Ma dated by Thompson et al., 2015). Earlier episodic deformation is characterized by distributed folding and faulting of the Cenozoic strata in the piggyback basin. In contrast, later (<5-6 Ma) deformation is primarily expressed by slip on the PFT upper ramp. Activity on previously-formed structures slowed or even ceased, and subsequently, were passively buried by deposits sourced from the Pamir range and the PFT hanging wall.

5.2. The Tuomuluoan Thrust

We initially describe the Tuomuluoan Thrust where it lies close to the epicenter of the 1985 Wuqia earthquake (Figure 3a). The fault has a ~25-km-long, northwest-trending arcuate surface trace. Where observed in outcrops, the fault places Paleogene gypsum along a 5-14°-dipping fault plane over Pleistocene Xiyu conglomerate of the Mingyaole anticline (J. Chen et al., 2005b): a box-like detachment fold belonging to the southern Tian Shan thrust system (Figures 5c & 7; T. Li et al., 2015). The Quaternary slip rate of the fault is as high as 6-7 mm/a (T. Li et al., 2012). Along the front of the thrust, the SE-flowing Kezilesu River is entrenched into a narrow valley, whose floor lies 600-900 m below the nearby Tuomuluoan topography.

In its western half, the Tuomuluoan upper ramp is characterized by a subhorizontal (~5°), bedding-parallel fault plane near the surface (Figure 7a). Downward, the ramp's dip abruptly increases to ~50°, then becomes gentler with a relatively consistent dip of ~19° before bending to the PFT flat at ~10 km depth. The dip of Tuomuluoan lower ramp, equal to that of the F1 ramp, is predicted (Shaw et al., 2005; Suppe, 1983) to be ~20° based on the dip ~23° of the kink band X_3-X_4. Likewise, ramp dips of both F2 and F3 are also estimated to be ~20°, thereby suggesting structural consistency among these ramps.

The slip along the Tuomuluoan and F1 flats is, respectively, ~5.8 km defined by the width of kink band Z_1-Z_2 and ~6.3 km according to displacement of the Mesozoic unit (Figure 7a; Table 2). Therefore, the Tuomuluoan lower ramp (which contributes slip both along the Tuomuluoan and the F1 flats) requires a total slip of ~14.5 km according to the fault-bend fold theory (Shaw et al., 2005; Suppe, 1983). Similarly, slip along the F2 ramp is estimated to be ~10 km. For the F3 ramp, the slip amount cannot be determined due to the poor quality of the seismic image. We assigned a likely slip of ~8.5 km based on the requirement that: (i) the Paleozoic strata are raised high enough to be exposed on the surface, and (ii) the maximum fault-throw magnitude of ~12 km of the hanging wall relative to the footwall. Overall, the summed slip along all deep ramps is ~33 km. Because the Paleogene strata are almost parallel with the underlying Tuomuluoan upper ramp and because the hanging-wall cutoffs above the fault have been eroded, we can only determine a minimum slip of ~18.5 km along the Tuomuluoan upper ramp.

Continuing eastward, the Tuomuluoan Thrust branches into two splays that are spaced 3-5 km apart on the surface (Figures 3 & 7b). The southern splay lies along the Tuomuluoan topographic front. Near the fault exposure, Paleogene strata are subvertical to overturned. We interpret this location to be close to the hanging-wall anticline which has been strongly eroded by the Kezilesu River. At depth, this fault has a shape similar to the Tuomuluoan ramp imaged on the profile *C* (Figure 7a). Although Quaternary activity is manifested by strongly folded fluvial gravels and proximal deposits in its footwall (Figure 5d), this splay did not slip during the 1985 Wuqia event (Feng, 1994). The northern splay, dipping ~26°S revealed by a fault exposure at the Kalangoulvke water gap, is located in the southern limb of the Mingyaole fold (Figures 3 & 5d). In contrast to the southern splay, the fault produced clear coseismic surface breaks during the Wuqia event (Feng, 1994). The formation of this fault appears to be very recent, because the geometry of the south-dipping Pliocene strata in its hanging wall is not significantly disturbed by the fault (Figure 7b). These two splays merge into one fault ramp dipping ~10-18° at 4-5 km depth. All lower ramps have a similar dip that is estimated to be ~18°. Cumulative slip along the Tuomuluoan lower ramp and faults F2 and F3 are ~17, 8, and 7.5 km, respectively (Figure 7b; Table 2). Based on the hanging-wall cutoff of the Paleogene strata, slip along the Tuomuluoan upper ramp is ~21-23 km, broadly consistent with the estimated slip of ≥18.5 km in its western half.

On profiles *C* and *D* (Figure 7), the location of the Tuomuluoan flat cutting down the section, ~40 km to the south of the fault exposure, is determined by the distance between hinges X_1 and X_2 (equal to the width of kink band Z_1-Z_2), the thickness of the Paleozoic-Mesozoic strata, and the F1 ramp dip of 18-20°.

5.3. The Transfer Fault and Kabajiate Thrust

To the west, the Tuomuluoan Thrust connects with an ~18-km-long, SE-trending transfer fault (Figure 3). At the Biertuokuoyi water gap, the transfer fault dips ~75°SW and displaces fluvial terraces and alluvial fans to create a series of SW-side-up fault scarps (Figure 5b1; T. Li et al., 2012). Slickensides preserved on the fault plane have rakes of ~33° (Figure 5b2), indicating the fault's dominant recent slip as a dextral oblique thrust. Based on displacement of dated fluvial terraces and the rake of slickensides, late Quaternary dip-slip and total-slip rates of the fault are estimated to be ~2.6 and 4.6 mm/a, respectively (T. Li et al., 2012; Thompson et al., 2018).

The subsurface geometry of the transfer fault (profile *B*: Figure 8b) reveals an upper ramp dipping ~59° near the surface. This ramp then becomes gentler to a dip of ~26°, which is steeper than the 18-19°-dipping Tuomuluoan upper ramp (Figure 7). Beneath the Pamir range, the lower ramp, and overlying F2 and F3 ramps are predicted to dip ~20° and to have slipped ~15.5, 10, and 12 km, respectively (Table 2). Slip along the upper ramp is ≥13 km because the hanging wall cutoff of the Paleogene strata has been totally eroded.

Farther west, strike-slip motion of the transfer fault is taken up by slip along the ESE-trending Kabajiate Thrust (Figure 3). Fault scarps along the fault trace are not as well developed as those along the transfer fault due to burial by young fluvial and alluvial deposits. Where exposed, Paleogene gypsum, limestone, and mudstone have been thrust over Miocene sandstone along a ~55°S-dipping fault plane (Figure 5a). ~20 km east of the fault outcrop, however, the fault plane is interpreted to have a much gentler, near-surface dip of ~11° (profile *A*: Figure 8a). At greater depths, the dip increases to ~33°, then decreases to ~22° across two gentle fault bends. The Kabajiate lower ramp, and the F2 and F3 ramps are estimated to have similar dips of ~17° and have experienced slips of ~20.5, 10, and 12.5 km, respectively (Table 2). Slip along the Kabajiate upper ramp is estimated to be ≥22 km. Compared to the transfer fault and the Tuomuluoan Thrust, the Kabajiate lower ramp contributes a much larger slip (~10 km) to the Kabajiate flat, consequently more material within the overlying fault blocks is transported across the synclinal fault bend fixed at hinge Z_1 and is raised to a higher structural level (Figures 7 & 8). Nonetheless, the cross-section geometry of the Kabajiate Thrust as a whole is similar in style to the transfer fault and the Tuomuluoan Thrust (Figures 7 & 8b).

On the profile *A* (Figure 8a), the top of the Kabajiate lower ramp is located ~48 km south of the fault exposure, indicating a southward step of ~8 km relative to the Tuomuluoan lower ramp. This step is likely accommodated by a sinistral strike-slip transfer fault between the Kabajiate and Tuomuluoan lower ramps, whose location is spatially correlated with the transfer fault on the upper ramp.

Immediately north of the Kabajiate thrust (Figures 3 & 8a), the surface-emergent, north-dipping Wulagen Thrust and its associated hanging-wall anticline expose Proterozoic rocks on the surface, representing the deformation front of the southern Tian Shan thrust system (Sobel et al., 2013; Thompson Jobe et al., 2017). Farther west, the Wulagen Thrust appears to be overridden by the Kabajiate Thrust (Figure 3). Despite strong interference of these two opposite-vergence thrust faults, the Paleozoic through Quaternary strata between these faults is flat or gently deformed.

Our interpretation also indicates that the Takegai Thrust in the basin is restricted within the Cenozoic sequence (Figure 8): a contrast with previous interpretations that the fault cuts through the Proterozoic basement and roots at depth beneath the Pamir (e.g., H. Chen et al., 2010; Cheng et al., 2016).

5.4. The Aismaola Thrust and Mushi Anticline

The Tuomuluoan Thrust, at its eastern end, is aligned obliquely with the Aismaola Thrust and the Mushi anticline (Figure 3). The Aismaola Thrust produces ESE-trending, ~10-km-long topographic relief in its hanging wall that comprises intensely deformed Paleogene and Miocene strata, and gently south-dipping Pliocene exposures. Its fault tip, however, is buried beneath modern fluvial deposits. Neither fault exposures nor clearly displaced geomorphic surfaces can be observed along the thrust fault’s approximate surface trace. Thompson Jobe et al. (2017), based on backtilting of fluvial terraces in its hanging wall, determined a late Quaternary slip rate of ≥0.7 mm/a along the Aismaola fault.

The dip of the Aismaola upper ramp decreases downward from ~46° to 24° across a gently curved fault bend (profile *E*: Figure 9a). The Aismaola flat (detachment horizon), localized at base of the Cenozoic sequence, has a measured dip of 3-4°, in contrast to the dip of ~0° of Tuomuluoan and Kabajiate flats. We propose that the hinterlandward dip of the Aismaola flat is attributable to flexural subsidence of the Tarim Basin due to overthrusting and loading by the Pamir range. Farther southwest, the Aismaola flat cuts down the section along a lower ramp, which dips ~18° according to the dip of kink band X_1-X_2. Dips of the F1, F2 and F3 ramps are assumed to be equal to that of the Aismaola lower ramp, considering that the F1, F2, F3 and the PFT lower ramp have similar dips at any of the profiles *A-D* (Figures 7 & 8). The slip along the Aismaola lower and upper ramps is determined to be ~6.5 and ≥14 km, respectively. We assign slip of 7.5, 7.0 and 8.0 km to the F1, F2 and F3 ramps (Table 2), respectively, because (i) as discussed in section 5.6, slip along the Aismaola lower ramp, F1, and F2 contributes to slip along the Aismaola upper ramp (≥14 km) and shortening of the Mushi anticline (~3 km, as described below), (ii) the Paleozoic strata are required to be raised and exposed on the surface, and (iii) total slip along these four ramps should be less than that at profiles *A-D*.

The Mushi anticline, exposing Pliocene strata in its core and Pleistocene Xiyu conglomerate on both limbs, has an elongate surface expression trending eastward for ~30 km (Figure 3). The fold has an asymmetric, north-vergent geometry (Figure 9a): its northern and southern limbs dip 60-70° and ~23°, respectively (T. Li et al., 2013). At depth, the fold is interpreted to be controlled by a blind thrust ramp. This ramp roots into a detachment horizon at ~6.5 km depth and ultimately merges with the Aismaola flat to the south. Total shortening of the fold is calculated to be ~3 km by the excess-area method (Epard & Groshong 1993), and its initiation age is ~2.1 Ma determined by burial cosmogenic dating of growth strata

(Thompson Jobe et al., 2018). Together, these estimates yield an average shortening rate of ~1.5 mm/a. This rate appears to continue into the late Quaternary, as documented by buckling deformation of fluvial terraces that has been quantified on its northern flank (T. Li et al., 2013).

In map view, the Aismaola Thrust and the Mushi fold step southward by ~10 and 3 km, respectively, when compared to the recently-activated northern Tuomuluoan Thrust (Figure 3). These steps are a logical necessity of a south-trending, dextral-slip transfer fault that links the Aismaola Thrust and Mushi fold with the northern Tuomuluoan Thrust. At depth, the top of the Aismaola lower ramp lies ~23 km south from the Aismaola exposure (Figure 9a). A sinistral strike-slip transfer fault is also required to accommodate the ~10-km forelandward step of the Aismaola lower ramp relative to that of the Tuomuluoan Thrust.

5.5. The Kumtagh Fault

As the easternmost segment of the PFT, the Kumtagh Fault is ~40 km long (Figure 3b). Starting from the eastern end of the Aismaola Thrust, the Kumtagh Fault crosses the north-flowing Ghez River and finally merges with the MPT at the Pamir range front (Figure 3). The fault’s northern half is almost totally buried beneath Quaternary alluvial and fluvial deposits. We define its form as a SE-trending, continuous fault strand based on seismic image observations. The fault gradually curves south and is well exposed along its southern half, where hanging wall Paleogene gypsum and mudstone are juxtaposed against Plio-Pleistocene Xiyu conglomerate in its footwall. Despite few unambiguous lateral offsets of geologic or geomorphic markers, we interpret the fault to be a presently active, dextral oblique thrust because it kinematically links the Aismaola Thrust and the Mushi anticline in the foreland basin with the MPT bounding the Pamir range to accommodate their differential basinward thrusting.

Seismic imaging only illustrates the shallow part of the northern half of the Kumtagh Fault (profile *F*: Figure 9b): its upper ramp is characterized by a listric fault plane, and its flat slopes toward the hinterland at an angle of ~3°, both of which are similar to the Aismaola Thrust. In its hanging wall, the core of its associated anticline is preserved. Dip slip along the upper ramp, therefore, can be well determined to be ~11 km according to the hanging-wall offset of the Paleogene strata. North of the Kumtagh Fault, the Mushi anticline shows a gentle, broad fold geometry with an ~12°-dipping southern limb and an ~26°-dipping northern limb. Its detachment horizon lies at ~5.5 km depth. Total shortening of the fold is ~3 km based on excess-area calculations.

No seismic profiles have been collected across southern half of the Kumtagh Fault. Here we use detailed surface mapping to extrapolate its subsurface geometry (Figure 9c). In the hanging wall, Paleogene and Miocene strata have a typical dip of ~46°. We interpret this dip to mimic that of the Kumtagh upper ramp. Westward across the Ghez River, the strata become horizontal across the synclinal hinge Z_1, then are overturned to dip ~65°SW across the synclinal hinge X_1, forming the SSE-trending, tight Kumtagh syncline. The synclinal hinge Z_1 can be fixed with the fault bend that separates the Kumtagh upper ramp from its flat lying along a detachment horizon at a depth of ~7 km. Slip along this ramp is estimated to be ≥12 km. Because stratal overturning on the Kumtagh western limb results from uplift and tilting by underlying stacked thrust ramps, we propose that lower ramps along profile *G* have a steeper fault dip or greater number of faults compared to those along profiles *A*-*E* (Figures 7-9).

On the profile *G* (Figure 9c), the synclinal hinge X_1 intersects with the detachment horizon ~18 km west of the fault exposure. This location approximately correlates with the top of the Kumtagh lower ramp. When combined with the top of the Aismaola lower ramp, a SE- to SSE-trending transfer fault with dextral oblique thrusting motion is likely present on the Kumtagh lower ramp.

5.6. Cenozoic Evolution of the Pamir Foreland Thrust System

Overall, the cross section of the Pamir thrust system in the study area is predominantly characterized by (i) four imbricated, basement-involved lower ramps (PFT, F1, F2 and F3) beneath the Pamir and (ii) one prominent, thin-skinned upper ramp (PFT) along with localized thrusts and folds in the foreland, all of which are connected by two (or one) detachment horizons (Figures 7-9). Deformation of the thrust system significantly raises the Pamir with respect to the foreland, such that the Paleozoic strata are widely exposed in the Pamir but are buried to depths of 7 to 9 km north of the thrust system.

Bed-length reconstructions determine an eastward decreasing total slip of the lower ramps from ~43 km at Kabajiate, to ~33 km at Tuomuluoan, and to ~29 km at Aismaola (Figure 3; Table 2). This slip contributes both to slip along the PFT upper ramp and to distributed thrusting and folding within the Biertuokuoyi piggyback basin (Figures 7-9). On profile *D* (Figure 7b), slip along the PFT lower ramp, F2 ramp, and F3 ramp is ~17, 8, and 7.5 km, respectively, and slip along the PFT upper ramp is ~21-23 km. Because slip along the PFT upper ramp can be approximately balanced by a total slip of ~25 km along the PFT lower ramp and F2 ramp, it is likely that (i) slip along the F3 ramp is not transferred to the PFT upper ramp, but is totally consumed by distributed deformation within the piggyback basin; and (ii) slip along the F2 ramp synchronously initiated with the activation of the PFT upper ramp around 5-6 Ma, as indicated by the regional angular unconformity (Thompson et al., 2015).

With this structural and geochronologic framework, we propose a break-forward sequence to illustrate Cenozoic evolution of the Pamir thrust system (Figure 10). In the first stage (prior to 5-6 Ma), the F3 ramp was formed and propagated basinward along the Cenozoic detachment, causing distributed deformation of the Cenozoic strata. This stage probably commenced concurrently with initiation age of 20-25 Ma of the northern Pamir (Sobel & Dumitru, 1997; Sobel et al., 2013). Since around 5-6 Ma (stages II and III), the F2 ramp broke forward followed by the F1 ramp, both of which flatten to the Cenozoic detachment. The slip along these two ramps is almost totally transferred to the PFT upper ramp, and deformation within the piggyback basin weakened significantly. The onset of this later stage is recorded by the regional angular unconformity in the piggyback basin (Figures 7-9). During the last stage (IV), the PFT lower ramp at the Kabajiate-Tuomuluoan segment slipped along the lower part of the F1 ramp and bent to activate the Paleozoic (lower) detachment, rather than rising upward to the Cenozoic (upper) detachment (Figure 10a). The upper part of original F1 ramp was intercepted and passively transported forelandward, while the Cenozoic detachment was refolded and raised. Most of the lower-ramp slip is transferred to the PFT upper ramp as well. Along the Aismaola segment (Figure 10b), contrastingly, the PFT lower ramp formed in front of the F1 ramp and continued to flatten to the Cenozoic detachment due to the lack of an efficient Paleozoic detachment. Aside from the PFT upper ramp, the lower-ramp slip is partially consumed by the Mushi anticline.

6. 3D Fault-Plane Geometry of the Pamir Frontal Thrust

The PFT upper ramp (including the Mushi anticline), the basal detachment, and the PFT lower ramp that formed in the latest break-forward sequence constitute the presently active thrust sheet of the Pamir thrust system (Figures 7-9). For the purpose of determining the rupture patch during the 1985 Wuqia earthquake sequence, we synthesize these cross sections and intervene surface data to reconstruct the 3D fault-plane geometry of the thrust sheet (Figure 11b).

The PFT upper ramp has a fairly sinuous fault trace on the surface (Figure 3) and is highly segmented at depth as is well constrained via interpretations of the seismic profiles (Figure 11b): from west to east, it includes the thrusting-dominated Kabajiate, Tuomuluoan, and Aismaola upper ramps that exhibit a right-stepping en echelon pattern overall. These thrust ramps are connected by lateral ramps (transfer faults) with map-view lengths >10 km and dextral oblique thrust slip. The upper ramp flattens downward to the basal detachment across a broadly arcuate fault bend, and the foot of the upper ramp is not as significantly segmented as its upper portion.

The basal detachment is localized at the base of the Paleozoic strata along the Kabajiate-Tuomuluoan segment, whereas it lies at the base of the Cenozoic strata along the Aismaola-Kumtagh segment due to the pinching out of the Paleozoic-Mesozoic strata (Figures 7-9, 11b). Its burial depth is ~12 km at its westernmost extent and gradually decreases to ~6 km to the east. Although located at different stratigraphic units and burial depths, the detachment horizon is relatively smooth and slopes gently to the west overall (Figure 11b).

Our interpretations also illustrate the significant segmentation that characterizes the PFT lower ramp, in spite of its relatively constant dip of 17-22° (Figures 7-9, 11b). From west to east, the Kabajiate lower ramp steps ~8 km north to the Tuomuluoan lower ramp, then steps ~10 km farther north to the Aismaola lower ramp. These lower ramps exhibit a left-stepping pattern overall, and the lateral ramps connecting them display sinistral strike-slip motion, contrasting with the upper ramp. Such a stepping pattern, however, is not clearly expressed in surface exposures of overlying Paleozoic strata (Figure 3): an ambiguity probably due to overlap between the most recent deformation and the significant pre-Cenozoic deformation of these strata. Because each segment of the lower ramp is spatially correlated with that of the upper ramp above the basal detachment, segmentation of the PFT lower ramp is responsible for or at least partially contributes to segmentation of its upper ramp.

Overall, our 3D fault-plane geometry indicates that the PFT thrust sheet is highly segmented both in its upper and lower ramps (Figure 11b): a segmentation with clear implications for seismicity on this portion of the PFT.

7. Seismicity

7.1. The 1985 Wuqia Earthquake

The 1985 ~M_w 6.9 Wuqia earthquake (mainshock, event 18) occurred near the surface trace of the Tuomuluoan segment of the PFT (Figure 3a; Table 1; note that the epicentral location may be off by >20 km). This earthquake was preceded by a M_w 5.0 foreshock (event 17, four hours earlier) near the transfer fault between the Tuomuluoan and Aismaola thrusts. Approximately 20 days later, the largest aftershock (M_w 5.9-6.1, event 20) occurred near the eastern end of the Tuomuluoan Thrust. Until the end of 1985, total recorded aftershocks include 8 events with magnitudes of ≥5.0 and more than 100 events with magnitudes of ≥3.0 (http://www.csi.ac.cn). This earthquake produced not only seismic-shaking induced rockfalls, landslides, and soil liquefaction, but also a spectacular ~15-km-long surface break zone along the eastern half and northern branch of the Tuomuluoan Thrust that was characterized by thrust scarps, strike-slip offsets, and pressure ridges, as well as secondary tension fissures in a few locations (Figure 3; Feng, 1994). Vertical and total displacements of the surface break were typically 0.5-1.5 m and 1-3 m, respectively. The surface break zone cannot be identified, however, where it cuts through the bedrock relief in the Tuomuluoan western half. A macroseismic field survey carried out by Feng (1994) documented that the isoseismic contours had major axes orientated subparallel with the PFT surface trace; the seismic intensity reached levels VIII and IX that are localized in an area of ~60 km long by ~10 km wide near the Tuomuluoan and Aismaola thrusts (Figure 2).

Due to sparse local seismic stations operating during the earthquake, seismologic studies only provide loose constraints on the seismic parameters (Figure 3a; Table 1). According to the U. S. Geological Survey (http://earthquake.usgs.gov/earthquakes/) and Harvard centroid-moment tensor (http://www.globalcmt.org/CMTsearch.html) catalogs, the earthquake was a M_w 6.9-7.0 oblique thrusting event with a strike/dip/rake of ~315°/29°/159° (one nodal plane solution of event 18a in Figure 3a; Table 1). Reanalysis of Burtman & Molnar (1993) and Fan et al. (1994) determined moment magnitudes of ~6.9, and focal mechanisms with strikes of ~298-316°, dips of ~44-46° and rakes of 132-160° (events 18b & 18c in Figure 3a; Table 1). Although these results are generally similar, the strike, dip and rake likely have uncertainties as large as ±60°, ±15° (30% of the dip), and ±60°, respectively, referring to parameter uncertainties of the largest aftershock (event 20, described in the next paragraph) determined by Burtman & Molnar (1993). The centroid depth is estimated at 10-25 km (Table 1), but a depth shallower than 10 km cannot be precluded (Burman & Molnar, 1993; Fan et al., 1994; Harvard CMT catalog).

Aside from the mainshock, focal mechanisms of the M_w 5.0 foreshock (event 17), a M_w 5.2 aftershock (event 19), and the largest aftershock (M_w 5.9-6.1, event 20) have been collected (Figure 3a; Table 1). The foreshock is a strike-slip faulting event, and two nodal planes of its focal mechanism indicate that the ruptured fault is either a SE-striking, dextral strike-slip fault or a NE-striking, sinistral strike-slip fault. The focal mechanism of the M_w 5.2 aftershock indicates that it is likely a gently south-dipping (~27°) or a steeply north-dipping (~66°) thrust event. For the largest aftershock, different researchers or organizations (e.g., Burtman & Molnar, 1993; Fan et al., 1994; Global CMT; U. S. Geological Survey) provide focal mechanisms with strikes of 108+30/-60°, dips of 31+7/-10°, and rakes of 104+25/-60°, and a centroid depth of 7±3 km.

7.2. Other Major Earthquakes on the Pamir Frontal Thrust

Besides the 1985 Wuqia earthquake, more than sixty events with magnitudes of ≥5.0, including seven ≥6.5 events, have been recorded and probably occurred on the PFT (Figure 2).

The 2008 M_w 6.6 Nura event (event 31), ~120 km west of the 1985 Wuqia event, is the most recent large earthquake triggered by the PFT (Figure 2; Table 1). This event was well recorded by the TIPAGE seismic network (Sippl et al., 2014): the focal depth is determined to be only 3-4 km; the focal mechanism indicates an ~59°S-dipping thrust. The Nura event produced a ~7-km-long surface break, including steep scarps and fractures with vertical offsets up to 0.8 m and identifiable sinistral displacement (Teshebaeva et al., 2014).

Approximately 120 km farther west from the Nura event (Figure 2; Table 1), the 1978 M_w 6.6 Zaalay event (event 9) was dominated by east-trending, dextral-slip faulting, in contrast with the thrust-dominated mechanisms of the Wuqia and Nura events. Given its focal mechanism solution, epicentral location, and neighboring structural characteristics, Arrowsmith & Strecker (1999) suggested that this event, with a focal depth of ~10 km, occurred on a transfer fault linking discontinuous thrust-dominated segments of the PFT.

The 1974 M_w 7.1 Markansu event (event 4) was the largest instrumental earthquake at the Pamir front (Figure 2; Table 1). This event was located <10 km southwest of the 2008 Nura event, according to the relocated epicenter of Sippl et al. (2014), and had a focal depth of only 2-5 km, as estimated by Fan et al. (1994) and Sippl et al. (2014). Its focal mechanism describes a slightly oblique reverse faulting event along an approximately NE-trending, steeply (~51°) SE-dipping fault plane. This event was followed by 13 aftershocks with M ≥5.0, including the M_w 5.8 event 5 and the M_w 5.9 event 6. In spite of high seismic moment release and shallow focal depth, the Markansu event did not produce a clear surface break, but triggered rather widespread landslides and discontinuous surface fractures, suggesting that the coseismic fault slip was consumed by distributed hanging-wall folding deformation during its upward propagation.

Additionally, according to instrumental and historical records, several large earthquakes, including the 1963 M 6.5 event, the 1955 M 6.9 and M 7.1 events, and the 1944 M 7.0 event, were located near the PFT (Figure 2). Because of the large uncertainty in their locations, unknown focal mechanism solutions, and the lack of relevant surface breaks, it remains unknown whether they occurred on the PFT or other active structures, such as the southern Tian Shan foreland thrust system and/or the Kongur Extensional System within the Pamir.

8. Discussion

8.1. Segmentation of the PFT and the 1985 Wuqia Earthquake Sequence

Through interpretations of surface mapping data and seismic reflection profiles, we reconstruct the 3D fault-plane geometry of the PFT near the 1985 Wuqia earthquake (Figure 11b). At depth, the fault includes upper and lower ramps that are separated by a ~15-km-wide basal detachment. Along strike, the PFT upper ramp is significantly segmented by transfer faults or lateral ramps with map-view lengths exceeding 10 km. Although all upper ramps merge onto the basal detachment, the lower ramp is highly segmented by ≥8-km-wide lateral ramps, as well. Because both of the upper and lower ramps are highly segmented along strike (as shown in Figure 1a) and considering that, for strike-slip and normal faults, a stepover with an along-strike width of ~5 km typically prohibits continuous propagation of the seismic rupture (e.g., Wesnousky, 2006, 2008; Zhang et al., 1999), these ≥8-km-wide transfer faults or lateral ramps are likely to serve as barriers for an earthquake sourced on any given segment of the thrusting-dominated fault patch.

During the 1985 Wuqia earthquake, the coseismic surface rupture was documented along the eastern half of the Tuomuluoan Thrust (Figure 3; Feng, 1994), indicating that the Tuomuluoan upper ramp was involved in the seismic rupture. The seismic moment magnitude is estimated to be 6.9-7.0 (Table 1; Burman & Molnar 1993; Fan et al., 1994; Harvard CMT catalog). According to the empirical scaling relationship between rupture area and seismic moment magnitude (Wells & Coppersmith, 1994), a best-fitting rupture area of 700-1000 km^2 is required. Correlating these two observations with our developed 3D fault plane geometry, we interpret two possible scenarios.

One possibility is that the 1985 Wuqia earthquake was sourced on the Tuomuluoan upper ramp and ruptured the entire fault patch (Figure 11): its along-strike length of ~25 km and downdip width of ~30 km are consistent with the required rupture area of 700-1000 km^2. Alternatively, the Wuqia earthquake was sourced on the lower ramp and ruptured the entire lower ramp, detachment and upper ramp (Figure 11a), which yields a total downdip rupture width of >45 km (~30 km of the upper ramp and ~15 km of the flat, and part of the lower ramp). This scenario seems less likely, because it is difficult to imagine that an earthquake sourced on the lower ramp with an along-strike length of ~25 km can release enough seismic moment to break through an ~15-km-wide detachment, an ~30-km-wide upper ramp, and ultimately to produce a coseismic slip of 1-3 m on the surface. Taking the Himalaya foreland thrust system as an example, where the thrust sheet is characterized by low dips and a large downdip width, all of the defined seismic rupture patches have a larger along-strike length than the downdip width (e.g., Avouac, 2015; Avouac et al., 2006; Mugnier et al., 2013; Elliott et al., 2016). Other examples, e.g., the 1999 M_w 7.6 Chi-Chi event, Taiwan (e.g., Dominguez et al., 2003; Yue et al., 2005) and the 2015 M_w 6.5 Pishan event at the Western Kunlun piedmont, China (e.g., Ainscoe et al., 2017; T. Li et al., 2015) also ruptured fault patches with larger along-strike lengths (versus downdip widths). Therefore, by analogy, we suggest that the coseismic rupture of the 1985 Wuqia event was likely encompassed within the Tuomuluoan upper ramp.

We recognize, however, that this interpretation is somewhat inconsistent with available focal mechanisms. According to the fault-plane solution of 298-316° strike, 44-46° dip and 132-160° rake provided by Burman & Molnar (1993), Fan et al. (1994) and Harvard CMT catalog, the conjugate fault-plane solution is 63-66° strike, 59-80° dip and 45-62° rake (Table 1), indicating a steeply NE-striking (SE-dipping) fault plane. However, the Tuomuluoan

Thrust is SE-striking (SW-dipping) and most of its upper ramp has dips of <20°(±6° uncertainty due to time-depth conversion). One speculative explanation of this contradiction lies in the large uncertainties of the focal mechanism. As documented by Burtman & Molnar (1993), the strike, dip, and rake of the NW-striking fault-plane solution have uncertainties of ±60°, ±15° and ±60°, respectively. If, for example, we use a rake of ~90°, the conjugate fault plane will be SE-striking (SW-dipping) and 30-60°-dipping. This strike is well consistent with the strike of the Tuomuluoan Thrust, and the dip approximately matches the average dip of the Tuomuluoan upper ramp if: (i) the steeper upper and western portion of the fault patch has experienced more significant rupture than its gentler lower and eastern portion (Figure 11b), which implies a relatively shallow centroid depth; and (ii) some lower part of the fault patch probably did not rupture during the mainshock, but ruptured during the M_w 5.2 and the M_w 5.9-6.1 aftershocks, both of which have relatively gently south-dipping (~27° and ~31+7/-10°, respectively; Table 1) fault-plane solutions. Based on our 3D fault-plane geometric model, the 1985 Wuqia mainshock probably has a focal mechanism of SE-striking, gently-dipping (probably 30-40°) and thrust-dominated, and has a relatively shallow centroid depth (probably <10 km).

Overall, we propose that the Tuomuluoan upper ramp, bounded by transfer faults or lateral ramps along strike and the basal detachment at depth, likely corresponds to the rupture patch of the 1985 Wuqia earthquake (Figure 11b), suggesting significant control on the seismic rupture process exerted by along-strike and downdip segmentation of the fault patch (Figure 1a).

8.2. Seismic Hazards at the Pamir Front

At the eastern half of the PFT, approximately from the epicenter of the 1974 Markansu event to its eastern end (Figure 2), a basal detachment is present at the base of the Cenozoic sequence (with a typical depth of 8-13 km) and separates the upper ramp from the lower ramp (Figure 4; Sippl et al., 2014; Teshebaeva et al., 2014), causing significant downdip segmentation. Lateral variations of stratigraphic lithology and thickness, along with rotation of the compressional stress direction around the Pamir front (Jay et al., 2017; Pan et al., 2018), result in significant along-strike segmentation of the upper ramp and likely the lower ramp. The segmentation characteristics and the seismic behavior of the Tuomuluoan segment, therefore, might be broadened to characterize the entire eastern half of the PFT.

During the instrumental period, the 1974 M_w 7.1 Markansu event and the 2008 M_w 6.6 Nura event have been recorded in addition to the 1985 M_w 6.9 Wuqia event (Figure 2; Table 1). These moderate-magnitude events can be explained by significant along-strike and downdip segmentation of the PFT sheet: as illustrated in Figure 1a, each fault ramp can act as an independent seismic source and thereby will tend to circumscribe the seismic moment. Based on the above reasoning, we think that future maximum magnitudes of earthquakes sourced on the eastern half of the PFT are similar to the M_w 7.1 Markansu event.

Extending to the west of the 1974 Markansu event, the western half of the PFT is also significantly segmented at the surface (Arrowsmith & Strecker, 1999; Strecker et al., 2003). At depth, however, structural interpretations of Coutand et al. (2002) suggest that the fault dips downward without a prominent regional detachment horizon, and, therefore, exhibits unclear downdip segmentation. During the instrumental period, only one $M_w \geq 6.5$ event (the 1978 Zaalay event, event 9) has been recorded along this portion (Figure 2). Given the different subsurface geometry and lower seismic moment release during the past several decades compared to the eastern half of the PFT, its western half probably has a significantly larger creeping portion, but more likely is currently locked and has a longer seismic-cycle interval (Sippl et al., 2014). In the second scenario, earthquakes with moment magnitudes much larger than ~7.1 (the moment magnitude of 1974 Markansu event) cannot be precluded.

8.3. Cenozoic Deformation and Evolution of the Pamir Foreland Thrust System

Besides investigating the seismogenic behavior of the PFT, the geometric and kinematic model of the Pamir thrust system provides useful constraints on Cenozoic deformation and evolution of the northern Pamir.

In the western Tarim Basin, as mentioned in section 8.2, the existing regional detachment horizon is localized in the Paleogene strata, such that the Pamir thrust system is characterized by imbricated, basement-involved thrust ramps in underlying, pre-Cenozoic strata that are decoupled from the thin-skinned PFT upper ramp, Takegai Thrust, and Mushi anticline in Cenozoic strata (Figures 7-9). Comparatively, the lack of a regional detachment horizon in the Alai Valley apparently favors thrust faults to be basement-involved (thick-skinned) and distributed across the foreland basin (Coutand et al., 2002). These different deformation patterns may be attributed to the varied lithology and thickness of the Cenozoic sequence. In the Tarim Basin, Paleogene strata comprise thick gypsum, gypsiferous mudstone, and limestone (Figure 4). This lithologic combination acts as a more efficient detachment horizon in comparison to the thin gypsum, dolomite, and conglomerate alternating with thick mudstone of the Alai Paleogene strata (Coutand et al., 2002; Wang et al., 2016). In addition, the Tarim Cenozoic strata above the detachment are 6-8 km thick: up to twice as thick as the Alai Cenozoic strata (only ~4 km thick; Coutand et al., 2002). Both a more efficient detachment horizon and a thicker sediment sequence above the detachment horizon facilitate the development of a decoupled, thin-skinned, foreland thrust system in the western Tarim Basin (e.g., Dean et al., 2013; Wu & McClay, 2011).

The Pamir thrust system in the western Tarim Basin follows an overall break-forward evolutionary sequence (Figure 10). At the present time, its deformation is localized at its leading edge (T. Li et al., 2012; Thompson Jobe et al., 2017). In contrast, the deformation front in the Alai Valley stepped basinward prior to ~16 Ma, then progressively retreated to the Pamir range front after ~16 Ma, thereby displaying an out-of-sequence thrusting pattern (Coutand et al., 2002). We speculate the out-of-sequence thrusting in the Alai Valley dominates now, because the north-vergent Pamir thrust system was juxtaposed with the south-vergent southern Tian Shan thrust system as early as ~16 Ma (Coutand et al., 2002). Subsequently, increasing interference with the southern Tian Shan thrust system likely forced its deformation front to retreat. In the western Tarim Basin, however, the Pamir thrust system was widely separated from the southern Tian Shan thrust system until very recently (no earlier than 5-6 Ma of the PFT initiation age; Thompson et al., 2015). Such separation helped sustain a normal, break-forward thrusting sequence.

At the longitude of the Kabajiate Thrust, the total slip of all faults within the Pamir thrust system is ~43 km. Combining with its initiation age of 25-20 Ma determined from low-temperature thermochronology (Cao et al., 2013; Sobel & Dumitru, 1997; Sobel et al., 2013), the average slip rate of the Pamir thrust system is 1.7-2.2 mm/a. Since around 5-6 Ma, the cumulative slip amount is ~30 km, accounting for an accelerated average slip rate of ~5-6 mm/a. This rate is consistent with PFT's Quaternary slip rate of 4-7 mm/a determined by displaced Quaternary strata and deformed fluvial terraces (T. Li et al., 2012; Thompson Jobe et al., 2017, 2018). Therefore, the Pamir thrust system apparently experienced slow deformation during the Miocene, followed by rapid basinward propagation and significant acceleration of shortening rate since late Miocene-early Pliocene. A similar tectonic transition is also recorded in the Hetian fold belt (~300 km southeast of our study area) at the Western Kunlun front (Figure 2 inset; Cheng et al., 2017), and the Atushi-Kashi fold belt and Kuche fold belt (immediately northeast and ~600 km northeast of our study area, respectively) at the southern Tian Shan front (Heermance et al., 2008; Tian et al., 2016; Zhang et al., 2018), implying that the mountain-to-basin convergence surrounding the Tarim Basin has accelerated significantly since the late Miocene-early Pliocene.

Deflection of Paleozoic and Mesozoic sutures, truncation of Cretaceous and Paleogene facies, and systematic paleomagnetic rotations suggest that the northern Pamir has indented northward by ~300 km during the Cenozoic (Blayney et al., 2016; Burtman & Molnar, 1993; Cowgill, 2010; Schwab et al., 2004; Sobel & Dumitru, 1997). The Pamir thrust system along the Pamir northern flank is commonly assumed to play an important role in accommodating this indentation (e.g., Burtman & Molnar, 1993; Arrowsmith & Strecker, 1999; Sobel et al., 2013), given its ~10 mm/a Quaternary shortening rate (Arrowsmith & Strecker, 1999; T. Li et al., 2012; Thompson Jobe et al., 2017; Yang et al., 2008; Zubovich et al., 2010, 2016), its spatial coincidence with the updip projection of the subducting Asian slab (e.g., Schneider et al., 2013; Sippl et al., 2013), and no large thrust faults identified within the northern Pamir (e.g., Burtman & Molnar, 1993; Sobel et al., 2013). Our interpretation of the Pamir thrust system, however, determines a maximum hanging-wall uplift of ~12 km relative to the footwall and a maximum fault slip of ~43 km (Table 2): significantly lower than the assumed ~300 km of overthrusting. One possible explanation of this mismatch, as suggested by Sobel et al. (2013), is the oceanic-style subduction of the Asian lithosphere in which the entire Asian crust together with the mantle lithosphere descends beneath the Pamir, and only part of the upper crust is scraped off and accreted into the Pamir thrust system. In that scenario, our cross-section reconstructions of the upper crust would, therefore, greatly underestimate the total regional convergence. An alternative explanation is that the ~300 km Cenozoic indentation of the northern Pamir is accommodated by distributed thrust faulting and crustal thickening, as well as strike-slip faulting across the entire northern Pamir-Tian Shan deformation zone (Figure 2 inset), rather than accommodated by a localized concentration along the Pamir thrust system. According to seismic tomographic images (Sippl et al., 2013), the northern Pamir is interpreted to have a crustal thickness of >70 km at present, indicative of significant crustal thickening and shortening. Approximately synchronous with the Pamir's indentation, the southern Tian Shan and Chatkal Range began to uplift and experienced both significant crustal thickening and vertical exhumation (Bande et al., 2015, 2017; Burtman et al., 1996; Sippl et al., 2013; Sobel & Dumitru, 1997). During the same period, the Talas-Fergana Fault has accumulated ~60 km of dextral strike slip (Burtman et al., 1996). All these structures and mechanisms could have accommodated significant northward indentation of the Pamir.

9. Conclusion

A dense grid of petroleum industry seismic reflection profiles available at the Kabajiate-Kumtagh segment of the Pamir Frontal Thrust (PFT) provide a unique opportunity to investigate the geometric characteristics of the PFT and its association with the regional seismic hazards. Our synthesis of the 3D fault-plane geometry illustrates that this portion of the PFT is significantly segmented both by transfer faults or lateral ramps along strike and by a wide basal detachment at depth. During the 1985 Wuqia earthquake, the Tuomuluoan upper ramp was the likely rupture site, suggesting a significant control on seismic rupture process by along-strike and downdip segmentation of the thrust sheet. Specifically, we suggest that significant segmentation of either the upper or lower thrust ramp or of an intervening detachment horizon can strongly influence the spatial extent and moment magnitude of ruptures: less lateral segmentation promotes larger magnitude earthquakes.

On the basis of this investigation, we speculate that the PFT eastern half and western half have different seismic behaviors: due to significant structural segmentation of the eastern half, ruptures are expected to be typified by spatially limited events with moment magnitude of ≤7.1; whereas the western half probably hosts much larger events, because reduced segmentation allows both deep and shallow ramps to rupture synchronously in the large magnitude events.

Our study also provides critical constraints on the deformation pattern and Cenozoic evolution of the northern Pamir. (i) The thrust system has experienced rapid basinward propagation and significant shortening acceleration since the late Miocene-early Pliocene. (ii) Deformation characteristics and the evolving sequence of the thrust system stand in contrast to those from the nearby Alai Valley. (iii) Total shortening accommodated by the Pamir thrust system is ≤43 km: much less than the Pamir’s overall indentation of ~300 km.

Acknowledgements

This study was funded by China NSF (grants 41772196 and 41772221), by National S&T Major Project of China (Grant Number 2016ZX05003-001), by the National Key Research and Development Program of China (2017YFC1500100), by Guangdong Province Introduced Innovative R&D Team of Geological Processes and Natural Disasters around the

South China Sea (2016ZT06N331), and by the U. S. National Science Foundation (EAR 1050070). We thank W. Xiao and X. Yang for their help in the field work and X. Wang and X. Cheng for fruitful discussions. With the courtesy of the PetroChina Company, original seismic reflection profiles on profiles *A*, *C*, *D* and *E* (Figures 7-9) are allowed to be released to the public (Figures S2-S5 in supporting information). Other data used in this paper have been presented in the tables and figures. Critical and thorough reviews of the manuscript by J. Hubbard, R. Heermance, two anonymous reviewers, the Associate Editor O. Zielke, and the Editor M. Savage significantly improved the current version.

References

Ainscoe, E. A., Elliott, J. R., Copley, A., Craig, T. J., Li, T., Parsons, B. E., & Walker, R. T. (2017). Blind thrusting, surface folding, and the development of geological structure in the Mw 6.3 2015 Pishan (China) earthquake. Journal of Geophysical Research: Solid Earth, 122, 9359-9382. https://doi.org/10.1002/2017JB014268

Allen, M. B., Windley, B. F., & Zhang, C. (1993). Paleozoic collisional tectonics and magmatism of the Chinese Tien Shan, Central Asia. Tectonophysics, 220, 89-115.

Allen, M. B., Windley, B. F., & Chi, Z. (1999). Late Cenozoic tectonics of the Kepingtage thrust zone: Interactions of the Tien Shan and Tarim Basin, northwest China. Tectonics, 18(4), 639-654. https://doi.org/10.1029/1999TC900019

Arrowsmith, J. R., & Strecker, M. R. (1999). Seismotectonic range-front segmentation and mountain-belt growth in the Pamir-Alai region, Kyrgyzstan (India-Eurasia collision zone). Geological Society of America Bulletin, 111, 1665-1683. http://doi:10.1130/0016-7606(1999)111<1665:SRFSAM>2.3.CO;2

Avouac, J. P. (2015). Mountain building: From earthquakes to geologic deformation. In: Gerald Schubert (editor-in-chief), Treatise on Geophysics (2nd edition, Vol 6, pp. 381-432). Oxford: Elsevier.

Avouac, J. P., Ayoub, F., Leprince, S., Konca, O., & Helmberger, D. V. (2006). The 2005, Mw 7.6 Kashmir earthquake: sub-pixel correlation of ASTER images and seismic waveforms analysis. Earth and Planetary Science Letters, 249, 514-528. http://dx.doi.org/10.1016/j.epsl.2006.06.025

Avouac, J. P., Tapponier, P., Bai, M., You, H., & Wang, G. (1993). Active thrusting and folding along the northern Tien Shan and late Cenozoic rotation of the Tarim relative to Dzungaria and Kazakhstan. Journal of Geophysical Research, 98, 6755-6804.

Bande, A., Sobel, E. R., Mikolaichuk, A., & Torres Acosta, V. (2015). Talas-Fergana Fault Cenozoic timing of deformation and its relation to Pamir indentation. In: Brunet, M., McCann, T., & Sobel, E. (eds), Geological Evolution of Central Asian Basins and the Western Tien Shan Range. Geological Society, London, Special Publications, 427. http://doi:10.1144/SP427.1

Bande, A., Sobel, E. R., Mikolaichuk, A., Schmidt, A., & Stockli, D. F. (2017). Exhumation history of the western Kyrgyz Tien Shan: Implications for intramontane basin formation. Tectonics, 36, 163-180. http://doi:10.1002/2016TC004284

Bershaw, J., Garzione, C. N., Schoenbohm, L., Gehrels, G., & Li, T. (2012). Cenozoic evolution of the Pamir plateau based on stratigraphy, zircon provenance, and stable isotopes of foreland basin sediments at Oytag (Wuyitake) in the Tarim Basin (west China). Journal of Asian Earth Sciences, 44, 136-148. http://doi:10.1016/j.jseaes.2011.04.020

Blayney, T., Najman, Y., Dupont-Nivet, G., Carter, A., Millar, I., Garzanti, E., ... Vezzoli, G. (2016). Indentation of the Pamirs with respect to the northern margin of Tibet: Constraints from the Tarim basin sedimentary record. Tectonics, 35, 2345-2369. http://doi:10.1002/2016TC004222

Bufe, A., Bekaert, D., Hussain, E., Bookhagen, B., Burbank, D. W., Thompson Jobe, J. A., Chen, J., Li, T., Liu, L., & Gan, W. (2017). Temporal changes in rock-uplift rates of folds in the foreland of the Tian Shan and the Pamir from geodetic and geologic data. Geophysical Research Letters, 44, 10,977-10,987. http://doi:10.1002/2017GL073627

Burtman, V. S., & Molnar, P. (1993). Geological and geophysical evidence for deep subduction of continental crust beneath the Pamir. Geological Society of America Special Papers, 281, 1-76. https://doi.org/10.1130/SPE281-p1

Cao, K., Wang, G., van der Beek, P., Bernet, M., & Zhang, K. (2013). Cenozoic thermo-tectonic evolution of the northeastern Pamir revealed by zircon and apatite fission-track thermochronology. Tectonophysics, 589, 17-32. http://doi:10.1016/j.tecto.2012.12.038

Chapman, J., Carrapa, B., Ballato, P., DeCelles, P., Worthington, J., Oimahmadov, I., Gadoev, M., Ketcham, R. (2017). Intracontinental subduction beneath the Pamir Mountains: Constraints from thermokinematic modeling of shortening in the Tajik fold-and-thrust belt. Geological Society of America Bulletin, 129, 1450-1471. https://doi.org/10.1130/B31730.1

Chen, H., Zhang, F., Cheng, X., Liao, L., Luo, J., Shi, J., Wang, B., Yang, C. & Chen, L. (2010). The deformation features and basin-range coupling structure in the northeastern Pamir tectonic belt [in Chinese]. Chinese Journal of Geology, 45, 102-112.

Chen, J., Qu, G., Hu, J., & Feng, X. (1997). Arcuate thrust tectonics and its contemporary seismicity in the eastern section of the external zone of the Pamir [in Chinese]. Seismology and Geology, 19, 301-312.

Chen, J., Scharer, K. M., Burbank, D. W., Heermance, R., & Wang, C. S. (2005b). Quaternary detachment folding of the Mingyaole anticline, southwestern Tianshan [in Chinese]. Seismology and Geology, 27, 530-547.

Chen, J. & He, D. (2018). Geometry and kinematics of Pamir frontal thrust zone [in Chinese]. Chinese Journal of Geology, 53, 25-45. http://doi:10.12017/dzkx.2018.002

Cheng, X., Chen, H., Lin, X., Yang, S., Chen, S., Zhang, F., Li, K., & Liu, Z. (2016). Deformation geometry and timing of the Wupoer thrust belt in the NE Pamir and its tectonic implications. Frontiers of Earth Science, 10(4), 751-760. http://doi:10.1007/s11707-016-0606-z

Cheng, X., Chen, H., Lin, X., Wu, L., & Gong, J. (2017). Geometry and Kinematic Evolution of the Hotan-Tiklik Segment of the Western Kunlun thrust belt: Constrained by structural analyses and apatite fission track thermochronology. The Journal of Geology, 125(1), 65-82. https://doi.org/10.1086/689187

Coutand, I., Strecker, M., Arrowsmith, J., Hilley, G., Thiede, R., Korjenkov, A., & Omuraliev, M. (2002). Late Cenozoic tectonic development of the intramontane Alai Valley (Pamir-Tien Shan region, Central Asia): An example of intracontinental deformation due to the Indo-Eurasia collision. Tectonics, 21, 1053. http://doi:10.1029/2002TC001358

Cowgill, E. (2010). Cenozoic right-slip faulting along the eastern margin of the Pamir salient, northwestern China. Geological Society of America Bulletin, 122, 145-161. http://doi:10.1130/B26520.1

Davis, G. H., Reynolds, S. J., & Kluth, C. F. (2012). Structural geology of rocks and regions (3rd ed., p. 839). Hoboken: NJ: John Wiley.

Dean, S., Morgan, J., & Fournier, T. (2013). Geometries of frontal fold and thrust belts: Insights from discrete element simulations. Journal of Structural Geology, 53, 43-53. http://dx.doi.org/10.1016/j.jsg.2013.05.008

Department of Earthquake Disaster Prevention, State Seismological Bureau. (1995). Catalogure of historical strong earthquakes in China (1912 A.D. -1990 A.D.) [in Chinese with English abstract] (pp.637). Beijing: Seismological Press.

Dominguez, S., Avouac, J. P., Michel, R. (2003). Horizontal coseismic deformation of the 1999 Chi-Chi earthquake measured from Spot satellite images: Implications for the seismic cycle along the western foothills of central Taiwan. Journal of Geophysical Research 108 (B2), 2083. doi:10.1029/2001JB000951.

DuRoss, C., Personius, S., Crone, A., Olig, S., Hylland, M., Lund, W. & Schwartz, D. (2016). Fault segmentation: New concepts from the Wasatch Fault Zone, Utah, USA. J. Geophys. Res: Solid Earth, 121, 1131-1157. http://doi:10.1002/2015JB012519

Elliott, J. R., Jolivet, R., González, P. J., Avouac, J. P., Hollingsworth, J., Searle, M. P. & Stevens, V. L. (2016). Himalayan megathrust geometry and relation to topography Gorkha earthquake. Nature Geoscience, 9, 174-180.

Epard, J. L., & Groshong, R. H. (1993). Excess area and depth to detachment. The American Association of Petroleum Geologists Bulletin, 77(4), 1291-1302.

Fan, G., Ni, J., & Wallace, T. (1994). Active tectonics of the Pamirs and Karakorum. Journal of Geophysical Research, 99(B4), 7131-7160.

Feng, X. Y. (1994). Surface rupture associated with the 1985 Wuqia earthquake, in Xinjiang [in Chinese]. Research on Active Fault (3), p. 45-55. Beijing: Seismological Press.

Guilbaud, C., Simoes, M., Barrier, L., Laborde, A., Van der Woerd, J., Li, H., Tapponnier, P., Coudroy, T., & Murray, A. (2017). Kinematics of active deformation across the Western Kunlun mountain range (Xinjiang, China), and potential seismic hazards within the southern Tarim Basin. Journal of Geophysical Research-Solid Earth, 112, 10,398-10,426. http://doi: 10.1002/2017JB014069

Guzofski, C., Shaw, J., Lin, G., & Shearer, P. (2007). Seismically active wedge structure beneath the Coalinga anticline, San Joaquin basin, California. Journal of Geophysical Research, 112, B03S05. http://doi:10.1029/2006JB004465

Hamling, I., Hreinsdóttir, S., Clark, K., Elliott, J., Liang, C., Fielding, E., … Stirling, M. (2017). Complex multifault rupture during the 2016 M_w 7.8 Kaikōura earthquake, New Zealand. Science, 356, no. 6334. http://doi: 10.1126/science.aam7194

Harris, R. A., & Day, S. M. (1993). Dynamics of fault interaction: Parallel strike-slip faults. Journal of Geophysical Research, 98, 4461-4472.

Heermance, R., Chen, J., Burbank, D., & Wang, C. (2007). Chronology and tectonic controls of Late Tertiary deposition in the southwestern Tian Shan foreland, NW China. Basin Research, 19, 599-632. http://doi:10.1111/j.1365-2117.2007.00339.x

Heermance, R. V., Chen, J., Burbank, D. W., & Miao, J. J. (2008). Temporal constraints and pulsed Late Cenozoic deformation during the structural disruption of the active Kashi foreland, northwest China. Tectonics, 27, TC6012. https://doi.org/10.1029/2007TC002226

Hubbard, J., Shaw, J., & Klinger, Y. (2010). Structural setting of the 2008 Mw 7.9 Wenchuan, China earthquake. Bulletin of the Seismological Society of America, 100, 2713-2735. http://doi:10.1785/0120090341

Hubbard, J., Almeida, R., Foster, A., Sapkota, S., Burgi, P., & Tapponnier, P. (2016). Structural segmentation controlled the 2015 Mw 7.8 Gorkha earthquake rupture in Nepal. Geology, 44, 639-642. http://doi:org/10.1130/G38077.1

Jay, C. N., Flesch, L. M., & Bendick, R. O. (2017). Kinematics and dynamics of the Pamir, Central Asia: Quantifying surface deformation and force balance in an intracontinental subduction zone. Journal of Geophysical Research: Solid Earth, 122, 4741-4762. http://doi:10.1002/2017JB014177

Jia, C., Zhang, S., & Wu, S. (2004). Stratigraphy of the Tarim Basin and Adjacent Areas [in Chinese] (pp. 1063). Beijing: Science Press.

King, G., & Nabelek, J. (1985). Role of fault bends in the initiation and termination of earthquake rupture. Science, 228(4702), 984-987.

Kulikova, G. (2016). Source parameters of the major historical earthquakes in the Tien-Shan region from the late 19th to the early 20th century. PhD thesis, University of Potsdam (Potsdam).

Lease, R., Burbank, D. W., Zhang, H., Liu, J., & Yuan, D. (2012). Cenozoic shortening budget for the northeastern edge of the Tibetan Plateau: Is lower crustal flow necessary? Tectonics, 31, TC3011. https://doi.org/10.1029/2011TC003066

Li, T., Chen, J., Thompson, J. A., Burbank, D. W., & Xiao, W. P. (2012). Equivalency of geologic and geodetic rates in contractional orogens: New insights from the Pamir Frontal Thrust. Geophysical Research Letters, 39, L15305. https://doi.org/10.1029/2012GL051782

Li, T., Chen, J., Thompson, J. A., Burbank, D. W., & Yang, X. (2013). Quantification of three-dimensional folding using fluvial terraces: A case study from the Mushi anticline, northern margin of the Chinese Pamir. Journal of Geophysical Research, 112, B03S09. https://doi.org/10.1029/2006JB004362

Li, T., Chen, J., Thompson, J. A., Burbank, D. W., & Yang, H. (2015). Hinge-migrated fold-scarp model based on an analysis of bed geometry: A study from the Mingyaole anticline, southern foreland of Chinese Tian Shan. Journal of Geophysical Research: Solid Earth, 120(9), 6592-6613. https://doi.org/10.1002/2015JB012102

Li, T., Chen, J., Fang, L., Chen, Z., Thompson, J. A., & Jia, C. (2016). The 2015 M_w 6.4 Pishan earthquake: Seismic hazards of active blind wedge thrust system at the Western Kunlun range front, northwest Tibetan Plateau. Seismological Research Letters, 87(3), 601-608. https://doi.org/10.1785/0220150205

Li, T., Chen, J., Thompson Jobe, J. A., & Burbank, D. W. (2017). Active flexural-slip faulting: Controls exerted by stratigraphy, geometry, and fold kinematics. Journal of Geophysical Research: Solid Earth, 122, 8538–8565. https://doi.org/10.1002/2017JB013966

Li, T., Chen, J., Thompson Jobe, J. A., Burbank, D. W., Cheng, X., Xu, J., Li, Z., Zheng, W., & Zhang, P. (2018). Active bending-moment faulting: Geomorphic expression, controlling conditions, accommodation of Fold Deformation. Tectonics, 37, 1-29. https://doi.org/10.1029/2018TC004982

Li, Y., Jia, D., Wang, M., Shaw, J.H., He, J., Lin, A., Xiong, L., & Rao, G. (2014). Structural geometry of the source region for the 2013 Mw 6.6 Lushan earthquake: Implication for earthquake hazard assessment along the Longmen Shan. Earth and Planetary Science Letters, 390, 275-286. http://doi:10.1016/j.epsl.2014.01.018

Liu, L. (2016). Sedimentology records of the Cenozoic convergence between the Pamir and Tian Shan [in Chinese]. PhD thesis, Institute of Geology, China Earthquake Administration (Beijing).

Lozos, J., Oglesby, D., Duan, B., & Wesnousky, S. (2011). The effects of double fault bends on rupture propagation: A geometrical parameter study. Bulletin of the Seismological Society of America, 101, 385-398. http://doi:10.1785/0120100029

Molnar, P., & Deng, Q. (1984). Faulting associated with large earthquakes and the average rate of deformation in central and eastern Asia. Journal of Geophysical Research, 89, 6203-6227.

Mugnier, J., Gajurel, A., Huyghe, A., Jayangondaperumal, R., Jouanne, F., & Upreti, B. (2013). Structural interpretation of the great earthquakes of the last millennium in the central Himalaya. Earth-Science Reviews, 127, 30-47. http://dx.doi.org/10.1016/j.earscirev. 2013.09.003

Pan, Z., He, J., & Li, J. (2018). Contemporary crustal deformation within the Pamir plateau constrained by geodetic observations and focal mechanism solutions. Pure and Applied Geophysics, in press. https://doi.org/10.1007/s00024-018-1872-3

Rajendran, K., Parameswaran, R., & Rajendran, C. (2017). Seismotectonic perspectives on the Himalayan arc and contiguous areas: Inferences from past and recent earthquakes. Earth-Science Reviews, 173, 1-30. http://dx.doi.org/10.1016/j.earscirev. 2017.08.003

Reiners, P. W., & Brandon, M. T. (2006). Using thermochronology to understand orogenic erosion. Annual Review of Earth and Planetary Sciences, 34, 419-466.

Scharer, K. M., Burbank, D. W., Chen, J., Weldon, R. J., Rubin, C., Zhao, R., & Shen, J. (2004). Detachment folding in the southwestern Tian Shan-Tarim foreland, China: Shortening estimates and rates. Journal of Structural Geology, 26(11), 2119-2137. https://doi.org/10.1016/j.jsg.2004.02.016

Schneider, F. M., Yuan, X., Schurr, B., Mechie, J., Sippl, C., Haberland, C., Minaev, V., Oimahmadov, I., Gadoev, M., Radjabov, N., Abdybachaev, U., Orunbaev, S., & Negmatullaev, S. (2013). Seismic imaging of subducting continental lower crust beneath the Pamir. Earth and Planetary Science Letters, 375, 101-112. http://dx.doi.org/10.1016/j.epsl.2013.05.015

Schurr, B., Ratschbacher, L., Sippl, C., Gloaguen, R., Yuan, X., & Mechie, J. (2014). Seismotectonics of the Pamir. Tectonics, 33, 1501-1518. http://doi:10.1002/2014TC003576

Schwab, M., Ratschbacher, L., Siebel, W., McWilliams, M., Minaev, V., Lutkov, V., Chen, F., Stanek, K., Nelson, B., Frisch, W., & Wooden, L. (2004). Assembly of the Pamirs: Age and origin of magmatic belts from the southern Tien Shan to the southern Pamirs and their relation to Tibet. Tectonics, 23, TC4002. http://doi:10.1029/2003TC001583

Schwartz, D., & Coppersmith, K. (1984). Fault behavior and characteristic earthquakes: Examples from the Wasatch and San Andreas fault zones. Journal of Geophysical Research, 89, 5681-5698.

Shaw, J. H., Connors, C., & Suppe, J. (2005). Seismic Interpretation of Contractional Fault-Related Folds (Vol. 53) AAPG Studies in Geology Tulsa, OK: American Association of Petroleum Geologists.

Sippl, C., Schurr, B., Tympel, J., Angiboust, S., Mechie, J., Yuan, X., Schneider, F. M., Sobolev, S. V., Ratschbacher, L., & Haberland, C. (2013). Deep burial of Asian continental crust beneath the Pamir imaged with local earthquake tomography. Earth and Planetary Science Letters, 384, 165-177. http://dx.doi.org/10.1016/j.epsl.2013.10.013

Sippl, C., Ratschbacher, L., Schurr, B., Krumbiegel, C., Rui, H., Pingren, L., & Abdybachaev, U. (2014). The 2008 Nura earthquake sequence at the Pamir-Tian Shan collision zone, southern Kyrgyzstan. Tectonics, 33, 2382-2399. http://doi:10.1002/2014TC003705

Sobel, E. R., & Dumitru, T. A. (1997). Exhumation of the margins of the western Tarim basin during the Himalayan orogeny. Journal of Geophysical Research, 102, 5043-5064.

Sobel, E. R. (1999). Basin analysis of the Jurassic-Lower Cretaceous southwest Tarim basin, NW China. Geological Society of America Bulletin, 111, 709-724.

Sobel, E. R., Chen, J., & Heermance, R. V. (2006). Late Oligocene-Early Miocene initiation of shortening in the southwestern Chinese Tian Shan: Implications for Neogene shortening rate variations. Earth and Planetary Science Letters, 247(1-2), 70-81. https://doi.org/10.1016/j.epsl.2006.03.048

Sobel, E. R., Schoenbohm, L. M., Chen, J., Thiede, R., Stockli, D. F., Sudo, M., & Strecker, M. (2011). Late Miocene-Pliocene deceleration of dextral slip between Pamir and Tarim: Implications for Pamir orogenesis. Earth and Planetary Science Letters, 304, 36-378. http://doi:10.1016/j.epsl.2011.02.012

Sobel, E. R., Chen, J., Schoenbohm, L. M., Thiede, R., Stockli, D. F., Sudo, M., & Strecker, M. (2013). Oceanic-style subduction controls late Cenzoic deformation of the Northern Pamir orogen. Earth and Planetary Science Letters, 363, 204-218. http://dx.doi.org/10.1016/j.epsl.2012.12.009

Stockmeyer, J., Shaw, J., & Guan, S. (2014). Seismic hazards of multisegment thrust-fault ruptures: Insights from the 1906 Mw 7.4-8.2 Manas, China, earthquake. Seismological Research Letters, 85, 801-808. http://doi:10.1785/0220140026

Strecker, M. R., Hilley, G. E., Arrowsmith, J. R. & Coutand, I. (2003). Differential structural and geomorphic mountain-front evolution in an active continental collision zone: the NW Pamir, southern Kyrgyzstan. Geological Society of America Bulletin, 115, 166-181.

Sun, J. & Jiang, M. (2013). Eocene seawater retreat fromthe southwest TarimBasin and implications for early Cenozoic tectonic evolution in the Pamir Plateau. Tectonophysics, 588, 27-38. http://dx.doi.org/10.1016/j.tecto.2012.11.031

Suppe, J. (1983). Geometry and kinematics of fault-bend folding. American Journal of Science, 283, 684-721. http://doi:10.2475/ajs .283.7.684

Teshebaeva, K., Sudhaus, H., Echtler, H., Schurr, B., & Roessner, S. (2014). Strain partitioning at the eastern Pamir-Alai revealed through SAR data analysis of the 2008 Nura earthquake. Geophysical Journal International, 198, 760-774. http://doi:10.1093/gji/ggu158

Thompson, J. A., Burbank, D. W., Li, T., Chen, J., & Bookhagen, B. (2015). Late Miocene northward propagation of the northeast Pamir thrust system, northwest China. Tectonics, 34, 510-534. https://doi.org/10.1002/2014TC003690

Thompson Jobe, J. A., Li, T., Chen, J., Burbank, D., & Bufe A. (2017). Quaternary tectonic evolution of the Pamir-Tian Shan collision zone, northwest China. Tectonics, 36, 2748-2776. http://doi:10.1002/2017TC004541

Thompson, J. A., Chen, J., Yang, H., Li, T., Bookhagen, & B., Burbank, D. (2018). Coarse- versus fine-grain quartz OSL and cosmogenic ^{10}Be dating of deformed fluvial terraces on the northeast Pamir margin, northwest China. Quaternary Geochronology, 46, 1-15. https://doi.org/10.1016/j.quageo.2018.01.002

Thompson Jobe, J. A., Li, T., Bookhagen, B., Chen, J., & Burbank, D. (2018). Dating growth strata and basin fill by combining 26Al/10Be burial dating and magnetostratigraphy:

Constraing active deformation in the Pamir-Tian Shan convergence zone, NW China. Lithosphere, in press. https://doi.org/10.1130/L727.1

Tian, Z., Sun, J., Windley, B., Zhang, Z. Gong, Z., Lin, X., & Xiao, W. (2016). Cenozoic detachment folding in the southern Tianshan foreland, NW China: Shortening distances and rates. Journal of Structural Geology, 84, 142-161. http://dx.doi.org/10.1016/j.jsg.2016.01.007

Wang, C., Cheng, X., Chen, H., Ding, W., Lin, X., Wu, L., Li, K., Shi, J., & Li, Y. (2016). The effect of foreland palaeo-uplift on deformation mechanism in the Wupoer fold-and-thrust belt, NE Pamir: Constraints from analogue modeling. Journal of Geodynamics, 100, 115-129. http://dx.doi.org/10.1016/j.jog.2016.03.001

Wang, M., Jia, D., Shaw, J., Hubbard, J., Li, Y., & Liu, B. (2014). The 2013 Lushan earthquake: Implications for seismic hazards posed by the range front blind thrust in the Sichuan basin, China. Geology, 42, 915-918. http://doi: 10.1130/G35809.1

Wang, X., Suppe, J., Guan, S. W., Hubert-ferrari, A., & Jia, C. (2011). Cenozoic structure and tectonic evolution of the Kuqa foldbelt, southern Tianshan, China. In K. R. McClay, J. Shaw, & J. Suppe (Eds.), Thrust Fault-Related Folding (AAPG Mem) (pp. 215-243).

Wei, H. H., Meng, Q., Ding, L., & Li, Z. (2013). Tertiary evolution of the western Tarim basin, northwest China: A tectono-sedimentary response to northward indentation of the Pamir salient. Tectonics, 32(3), 558-575. https://doi.org/10.1002/tect.20046

Wells, D. L., & Coppersmith, K. J. (1994). New empirical relationships among magnitude, rupture length, rupture width, rupture area, and surface displacement. Bulletin of the Seismological Society of America, 94, 974-1002.

Wesnousky, S. G. (2006). Predicting the endpoints of earthquake ruptures. Nature, 444, 358-360. https://doi: 10.1038/nature05275

Wesnousky, S. G. (2008). Displacement and geomechanical characteristics of earthquake surface ruptures: Issues and implications for seismic-hazard analysis and the process of earthquake rupture, Bulletin of the Seismological Society of America, 98, 1609-1632. https://doi: 10.1785/0120070111

Windley, B. F., Allen, M. B., Zhang, C., Zhao, Z., & Wang, G. (1990). Paleozoic accretion and Cenozoic redeformation of the Chinese Tien Shan Range, central Asia. Geology, 18, 128-131. doi:10.1130/0091-7613(1990)018<0128:PAACRO>2.3.CO;2

Wu, J. E., & McClay, K. R. (2011). In K. R. McClay, J. Shaw, & J. Suppe (Eds.), Thrust Fault-Related Folding (AAPG Mem) (pp. 301-333).

Yang, S. M., Li, J., & Wang, Q. (2008). The deformation pattern and fault rate in the Tianshan Mountains inferred from GPS observations. Science in China Series D, 51(8), 1064-1080. https://doi.org/10.1007/s11430-008-0090-8

Yeats, R. S., Sieh, K. S., & Allen, C. R. (1997). Geology of Earthquake (p. 568). New York: Oxford University Press.

Yin, A., Nie, S., Craig, P., Harrison, T. M., Ryerson, F. J., Qian, X., & Yang, G. (1998). Late Cenozoic tectonic evolution of the southern Chinese Tian Shan. Tectonics, 17(1), 1-27. https://doi.org/10.1029/97TC03140

Yue, L., Suppe, J., & Hung, J. (2005). Structural geology of a classic thrust belt earthquake: the 1999 Chi-Chi earthquake Taiwan (M_w = 7.6). Journal of Structural Geology, 27, 2058-2083.

Zhang, P., Mao, F., & Slemmons, D. B. (1999). Rupture terminations and the size of segment boundaries from historical earthquake ruptures in the Basin and Range Province. Tectonophysics, 308, 37-52.

Zhang, Z., Sun, J., Lü, L, Wang, W., & Li, Y. (2018). Neogene paleomagnetic study of the western Baicheng Depression: Implications for the intensified deformation of the Tian Shan since the latest Miocene. Journal of Geophysical Research: Solid Earth, in press. http://doi:10.1029/2018JB016953

Zubovich, A., Schöne, T., Metzger, S., Mosienko, O., Mukhamediev, Sh., Sharshebaev, A., & Zech, C. (2016). Tectonic interaction between the Pamir and Tien Shan observed by GPS. Tectonics, 35, 283-292. http://doi:10.1002/2015TC004055

Zubovich, A., Wang, X., Scherba, Y., Schelochkov, G., Reilinger, R., Reigber, C., ... Beisenbaev, R. (2010). GPS velocity field of the Tien Shan and surrounding regions. Tectonics, 29, TC6014. https://doi.org/10.1029/2010TC002772

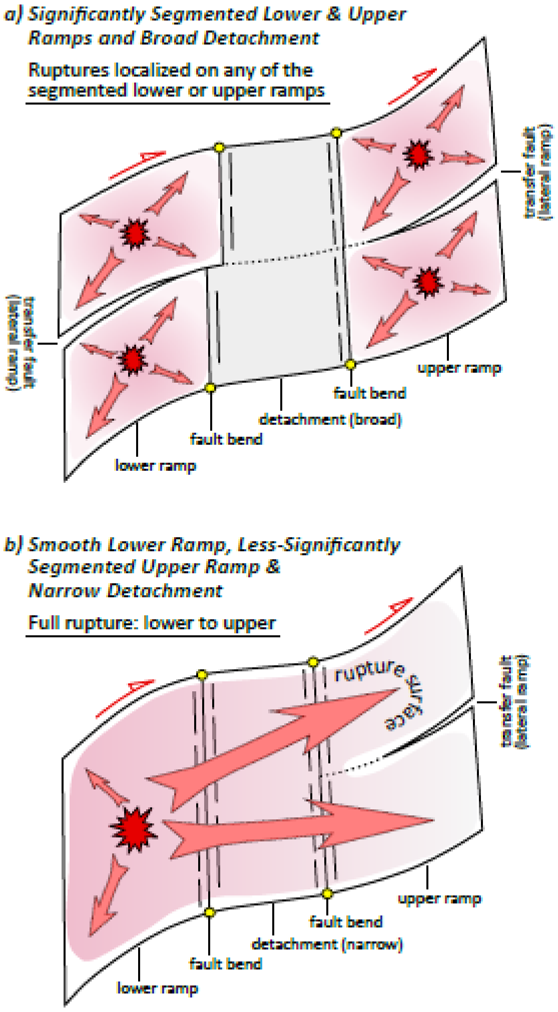

a) Significantly Segmented Lower & Upper Ramps and Broad Detachment

Ruptures localized on any of the segmented lower or upper ramps

b) Smooth Lower Ramp, Less-Significantly Segmented Upper Ramp & Narrow Detachment

Full rupture: lower to upper

Figure 1. Two contrasting seismic source models controlled by along-strike and downdip segmentation of a foreland thrust sheet that typically includes lower ramps, detachment horizons, and upper ramps. (a) If the lower and upper ramps are significantly segmented by lateral ramps and are separated by a broad detachment, the seismic moment release of each ramp segment is limited, such that the rupture is likely confined within individual ramps. The detachment may either rupture concurrently with the upper ramp (e.g., during the 1999 M_w 7.6 Chi-Chi event, Taiwan; Yue et al., 2005) or with the lower ramp, can act as a single source of earthquakes (e.g., during the 2015 M_w 7.8 Gorkha event, Nepal; Hubbard et al., 2016), or is not seismically active (e.g, Zagros thrust system, Iran; Yeats et al., 1997). Otherwise, (b) if the lower ramp is relatively smooth, the upper ramp is less-significantly segmented, and the detachment is relatively narrow, an earthquake sourced on the lower ramp can rupture the entire thrust sheet.

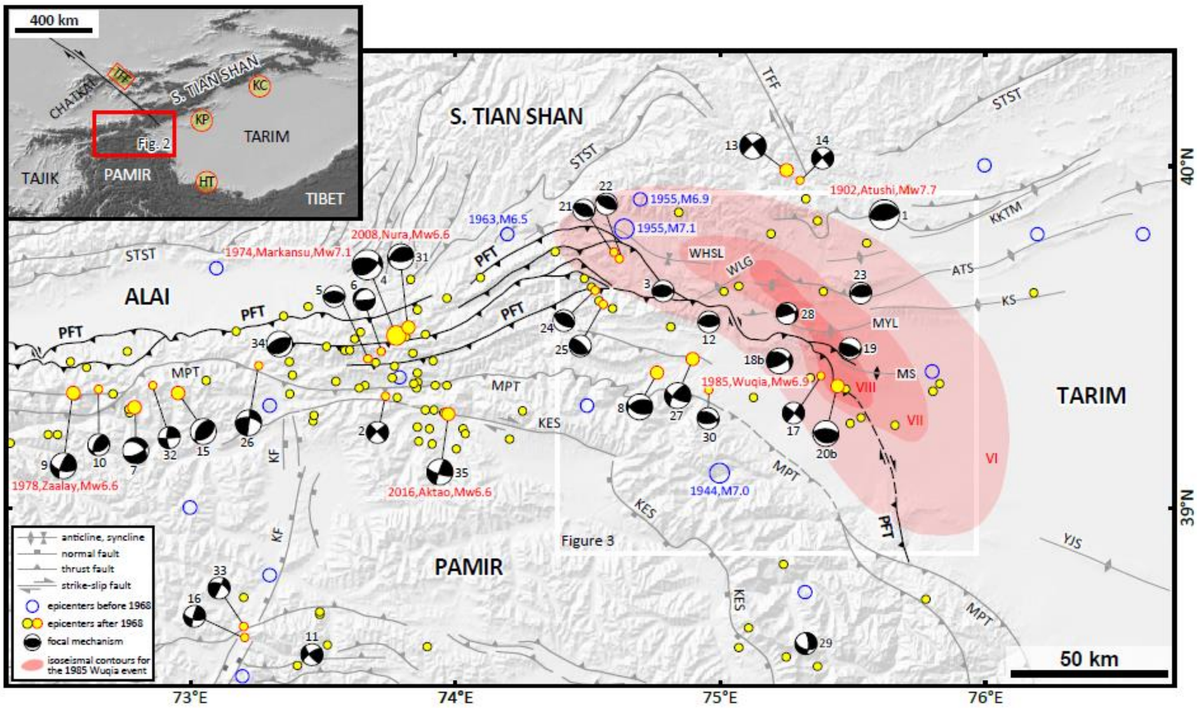

Figure 2. Major Cenozoic structures and seismicity at the Pamir front and adjacent areas. Inset map shows the location of this study area in Central Asia. Epicenter of the 1902 Atushi event (event 1) from Kulikova (2016); other epicenters (M≥5.0) before 1968 from GSHAP (Global Seismic Hazard Assessment Program, http://www.seismo.ethz.ch/static/GSHAP) seismic catalog and historical earthquake catalog in China (Department of Earthquake Disaster Prevention, State Seismological Bureau, 1995). Epicenters after 1968 from U. S. Geological Survey seismic catalog (http://earthquake.usgs.gov/earthquakes/) for the period 1968-2018. Focal mechanism solutions from Fan et al. (1994), Kulikova (2016), Sippl et al. (2014), and U. S. Geological Survey seismic catalog (detailed parameters listed in Table 1). Isoseismic contours for the 1985 Wuqia event from Feng (1994). ATS = Atushi anticline; HT = Hetian foreland thrust system; KC = Kuche fold belt; KES = Kongur Extensional System; KF = Karakul Fault; KKTM = Keketamu anticline; KP = Kepintagh fold belt; KS = Kashi anticline; MPT = Main Pamir Thrust; MS = Mushi anticline; PFT = Pamir Frontal Thrust; TFF = Talas-Fergana Fault; WHSL = Wuheshalu syncline; WLG = Wulagen anticline; YJS = Yingjisha anticline.

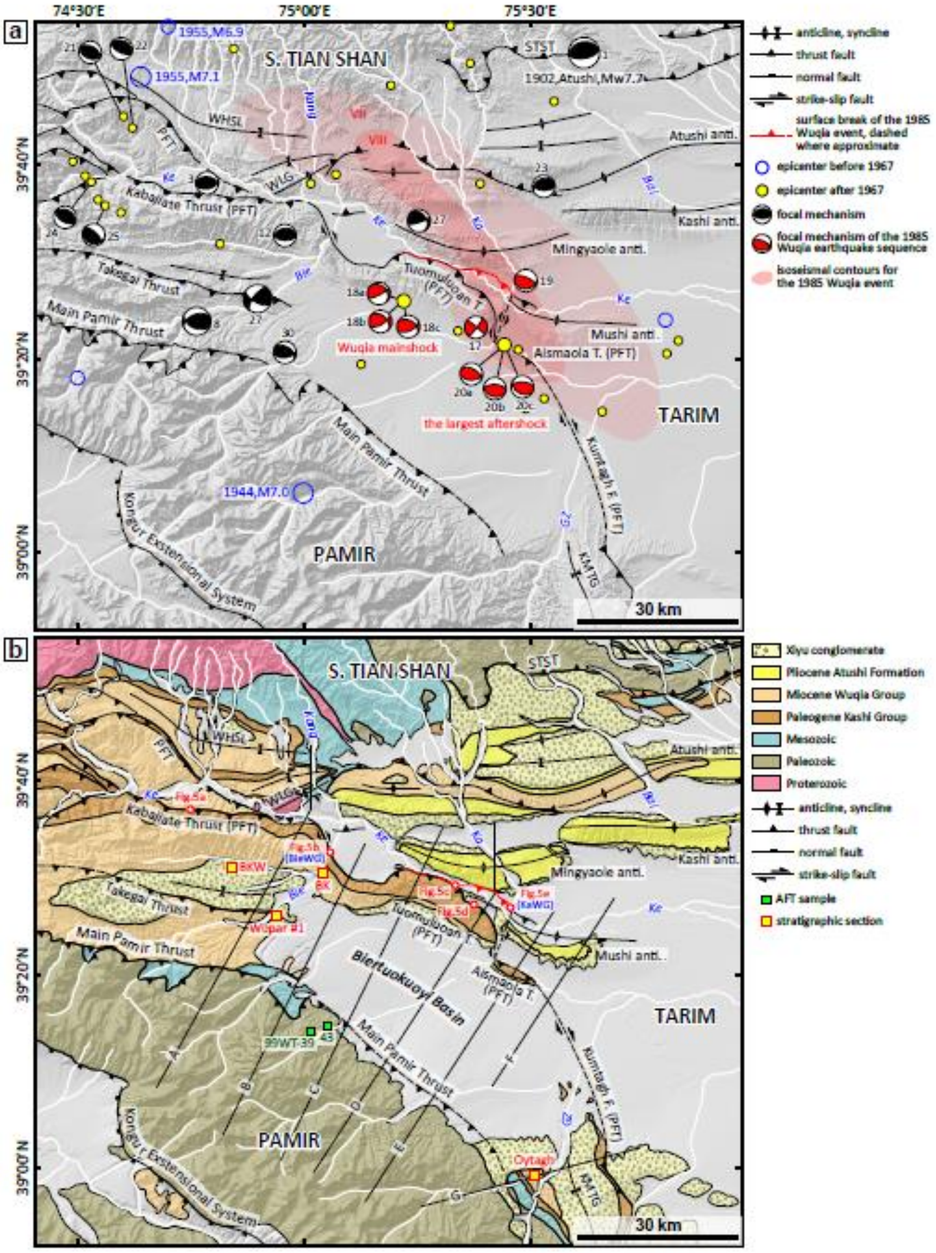

Figure 3. (a) Major Cenozoic structures and seismicity and (b) geologic map of the Pamir foreland thrust system and adjacent areas (modified from T. Li et al., 2017). Lines *A* to *G* depict locations of geological cross sections in Figures 7-9. See Figure 2 for the map location. BK = Biertuokuoyi section; BKW = Biertuokuoyi West section; KMTG = Kumtagh syncline; PFT = Pamir Frontal Thrust; STST = Southern Tian Shan Thrust; WHSL = Wuheshalu syncline; WLG = Wulagen anticline. Bai = Baishkeranmu River; Bie = Biertuokuoyi River; BieWG = Biertuokuoyi water gap; GZ = Ghez River; Ka = Kalangoulvke River; KaWG = Kalangoulvke water gap; Kang = Kangsu River; Ke = Kezilesu River.

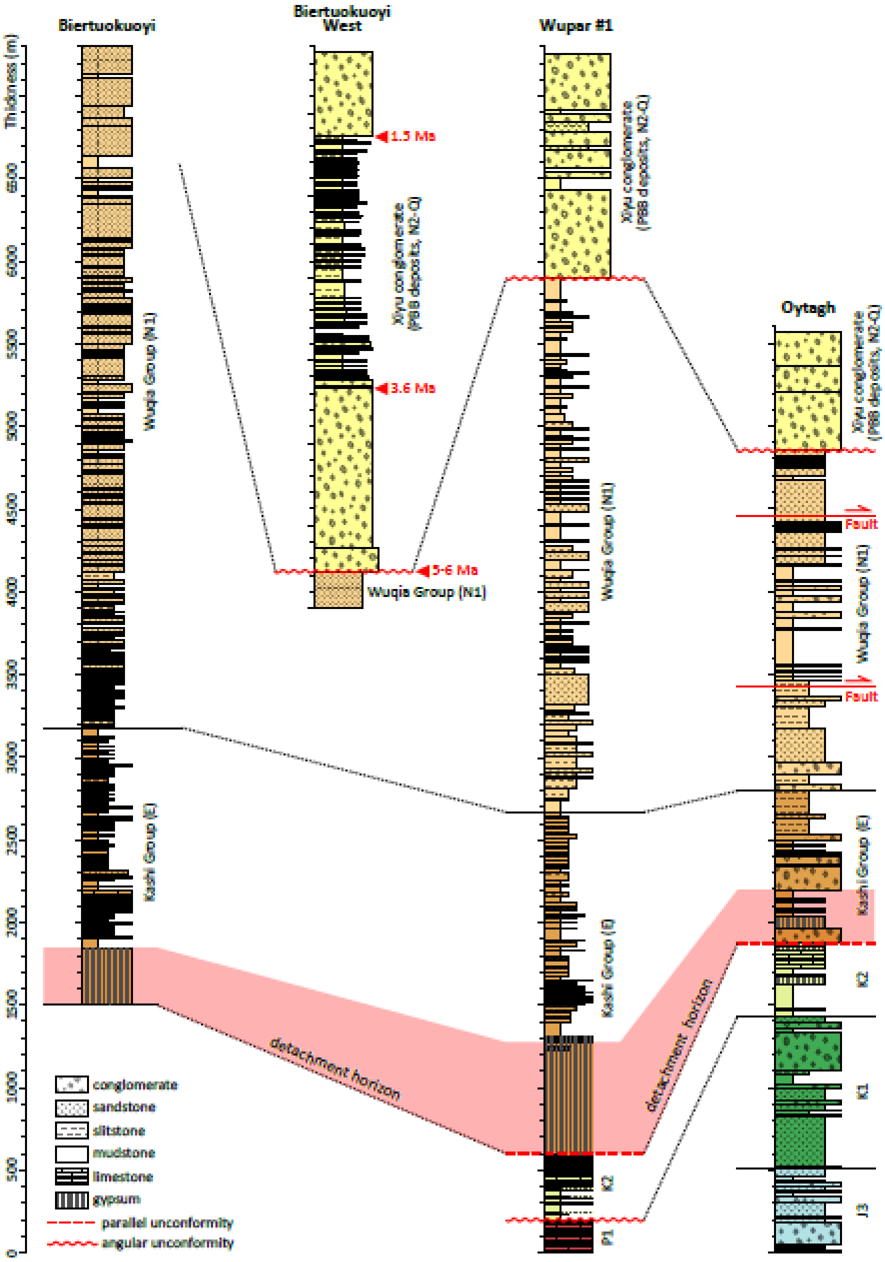

Figure 4. Stratigraphic columns in the study area. See Figure 3b for the section locations. Sections Biertuokuoyi, Biertuokuoyi West, and Oytagh modified from Bershaw et al. (2012), Liu (2016) and Thompson et al. (2015), and the section Wupar #1 modified from unpublished well-log data of borehole Wupar #1. The massive gypsum at the base of the Cenozoic sequence represents one of the regional detachment horizons of the Pamir foreland thrust system.

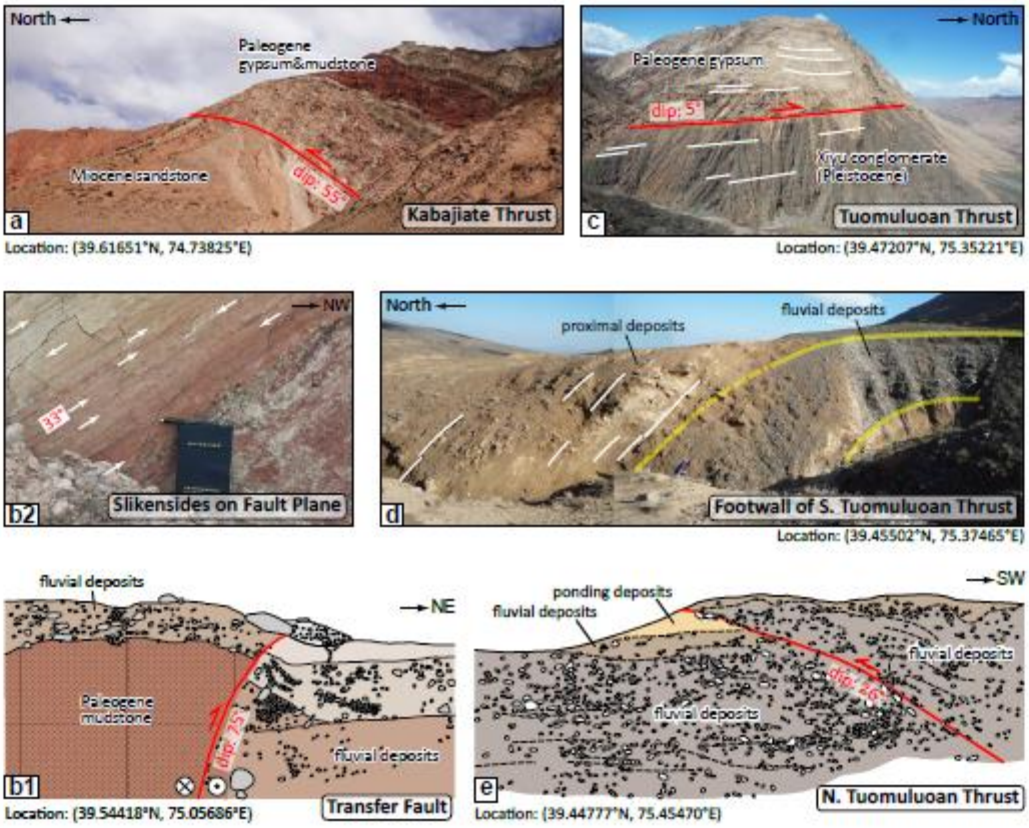

Figure 5. (a) Photograph of the Kabajiate Thrust outcrop. (b1) Sketch of the transfer fault outcrop at Biertuokuoyi water gap and (b2) Slickensides on the fault plane at the Biertuokuoyi water gap showing its dextral oblique thrust motion. (c) Photograph of the Tuomuluoan Thrust outcrop. The Xiyu conglomerate was dated to the Pleistocene by J. Chen et al. (2005). (d) Folded fluvial deposits and proximal deposits from the Tuomuluoan relief in the footwall of the southern Tuomuluoan Thrust. (e) Sketch of the northern Tuomuluoan Thrust outcrop at the Kalangoulvke water gap. See Figure 3b for locations of these photographs and sketches.

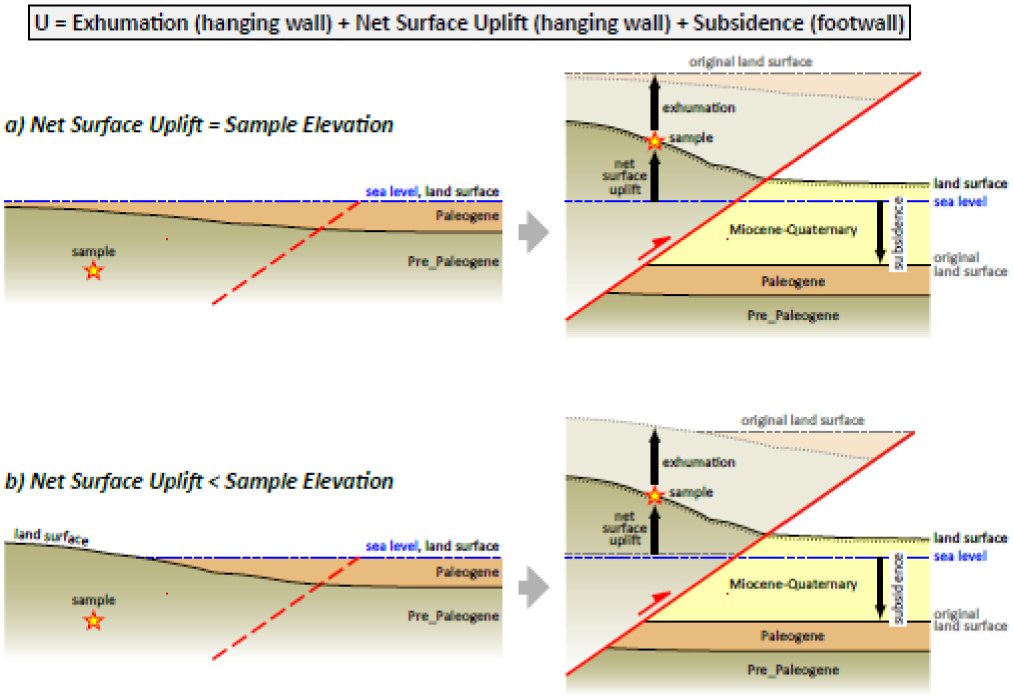

Figure 6. A simple model showing that the fault-throw magnitude (*U*) of the hanging wall relative to the footwall is equal to the sum of the hanging-wall exhumation, the hanging-wall net surface uplift, and the footwall subsidence. The upper boundary of the Paleogene unit was deposited originally at sea level. Above the sample location, (a) if the Paleogene strata were originally deposited near sea level, the hanging-wall net surface uplift is equal to the present elevation of the sample; (b) otherwise, if the Paleogene land surface sat above sea level, the hanging-wall net surface uplift is less than the present elevation of the sample.

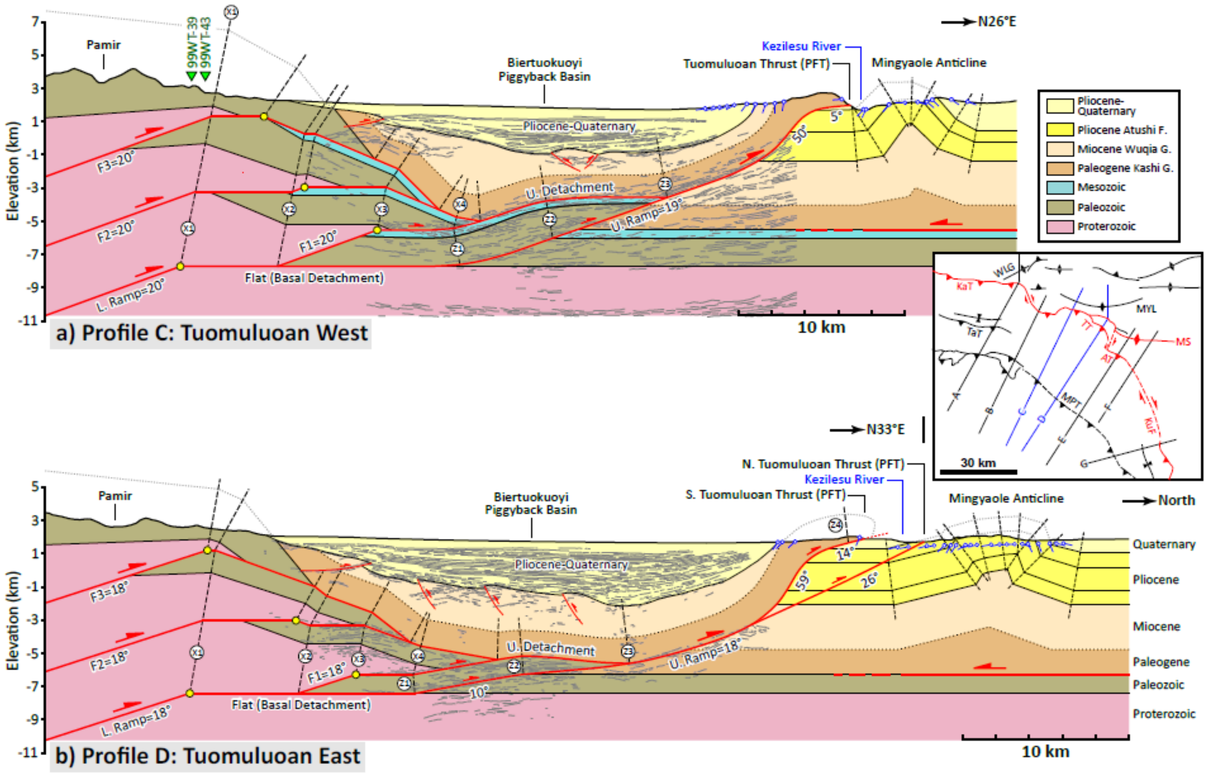

Figure 7. Geologic cross sections of the western (a) and eastern (b) Tuomuluoan Thrust interpreted from seismic reflection profiles and field mapping data (see inset map with blue colored lines and Figure 3b for locations). The depth conversion for two profiles assumes a uniform velocity of ~4000 m/s. Yellow circles mark the original transition locations from the lower ramp to the flat when each fault was active. Topography in the profiles from the SRTM DEM. Apatite fission-track samples 99WT-39 and 99WT-43 from Sobel et al. (2013) are correlated with the profile *C*. Cross sections of the Mingyaole fold refer to T. Li et al. (2015) and Scharer et al. (2004). See Figures S3 and S4 for the uninterpreted version of the seismic reflection profiles. AT = Aismaola Thrust; KaT = Kabajiate Thrust; KuF = Kumtagh Fault; MPT = Main Pamir Thrust; MS = Mushi anticline; MYL = Mingyaole anticline; TaT = Takegai Thrust; TT = Tuomuluoan Thrust; WLG = Wulagen anticline. L. Ramp = Lower Ramp; U. Ramp = Upper Ramp.

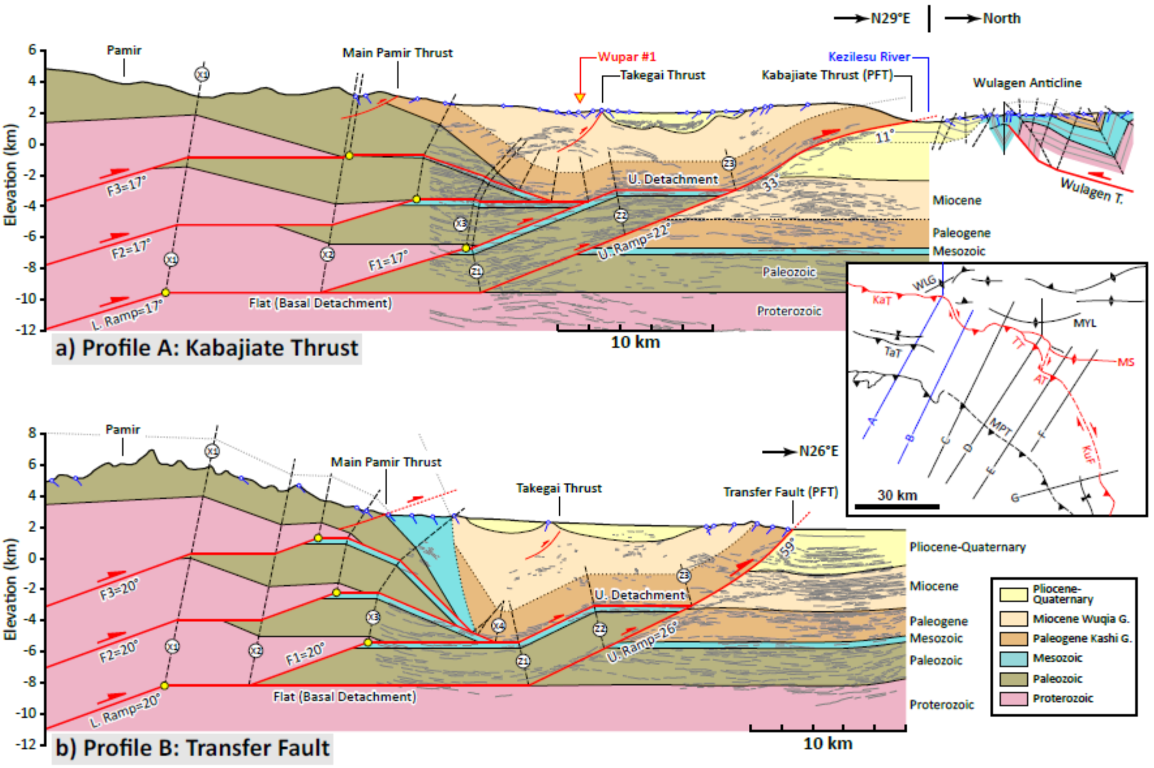
a) Profile A: Kabajiate Thrust

b) Profile B: Transfer Fault

Figure 8. Geologic cross sections of (a) the Kabajiate Thrust and (b) the transfer fault between Kabajiate and Tuomuluoan thrusts (see blue lines on inset map and Figure 3b for locations). Yellow circles mark original transition locations from the lower ramp to the flat. Topography in the profiles from the 90 m SRTM DEM. See Figure S2 for the uninterpreted version of the seismic reflection profile in profile *A*. AT = Aismaola Thrust; KaT = Kabajiate Thrust; KuF = Kumtagh Fault; MPT = Main Pamir Thrust; MS = Mushi anticline; MYL = Mingyaole anticline; TaT = Takegai Thrust; TT = Tuomuluoan Thrust; WLG = Wulagen anticline. L. Ramp = Lower Ramp; U. Ramp = Upper Ramp.

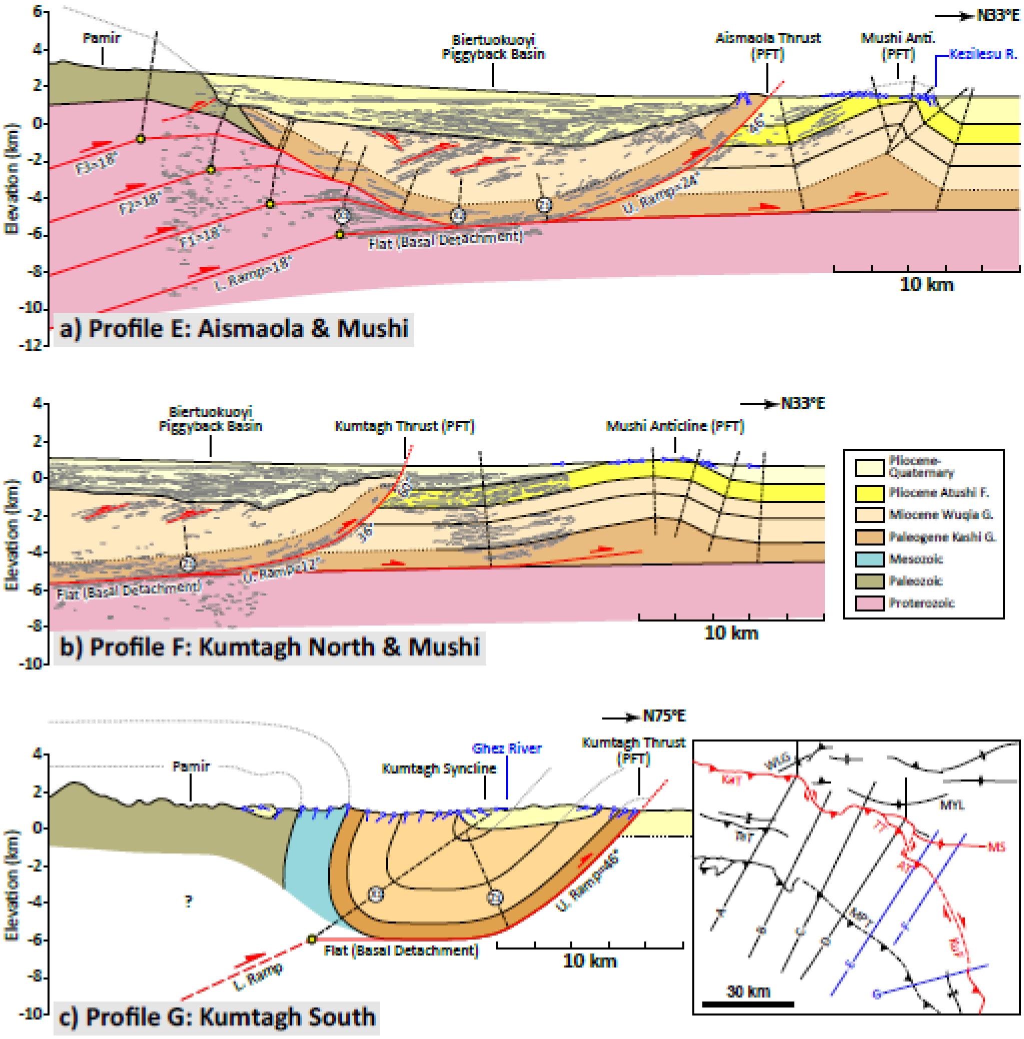

Figure 9. Geologic cross sections of (a) the Aismaola Thrust and the Mushi anticline, (b) the northern Kumtagh Thrust and the Mushi anticline, and (c) the southern Kumtagh Thrust interpreted by seismic reflection profiles and field mapping data (locations shown in inset map and Figure 3b). Yellow circles mark original transition locations from the lower ramp to the flat. Topography in the profiles from the SRTM DEM. Note that on profile *G*, the top of the Kumtagh lower ramp is assigned with the projection of the synclinal hinge X_1. See Figure S5 for the uninterpreted version of the seismic profile in profile *E*. AT = Aismaola Thrust; KaT = Kabajiate Thrust; KuF = Kumtagh Fault; MPT = Main Pamir Thrust; MS = Mushi anticline; MYL = Mingyaole anticline; TaT = Takegai Thrust; TT = Tuomuluoan Thrust; WLG = Wulagen anticline. L. Ramp = Lower Ramp; U. Ramp = Upper Ramp.

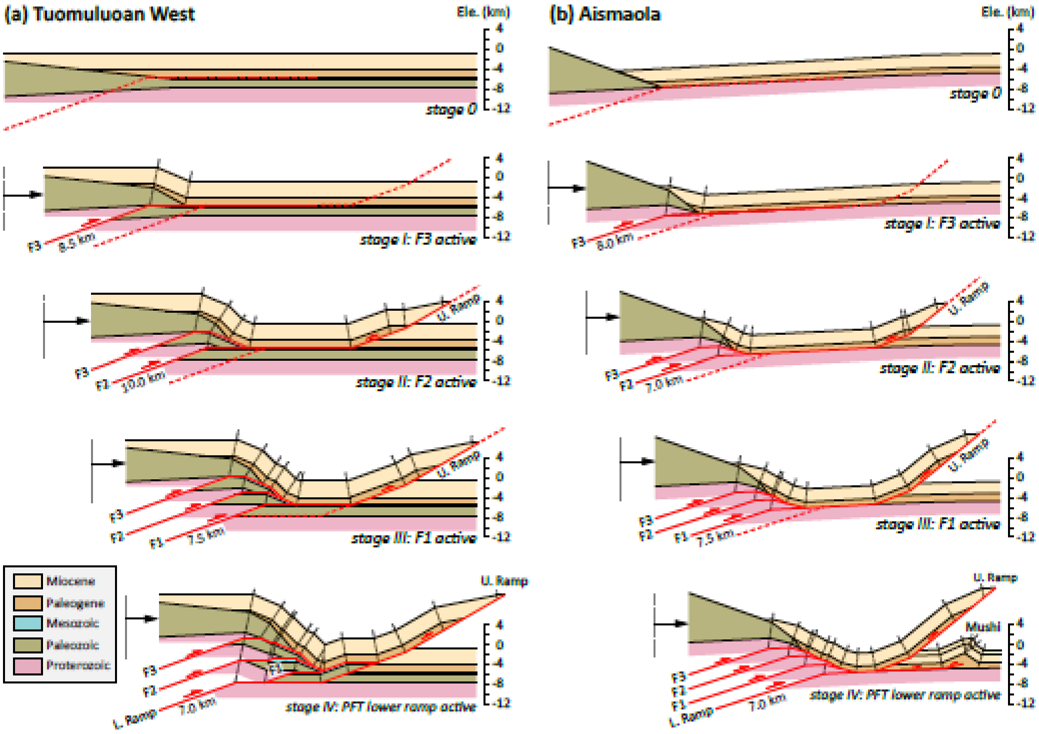

Figure 10. Schematic forward model of the Pamir thrust system at (a) Tuomuluoan West (Figure 7a) and (b) Aismaola (Figure 9a) (horizontal scale = vertical scale). Stage 0: Undeformed. Stage I: the F3 ramp active. Cenozoic strata in the foreland are deformed into distributed thrusts and folds, which are not shown in our model for simplifying the diagram. Stage II: F2 ramp active. The PFT upper ramp is formed synchronously with initiation of F2 ramp slip. Stage III: F1 ramp active. Stage IV: PFT lower ramp activates the Paleozoic detachment at Tuomuluoan West but continues to flatten to the Cenozoic detachment at Aismaola. The Mushi anticline is formed to the north of the PFT at Aismaola. Note that (i) the Paleozoic unit requires an original topography in the Pamir in order to be presently exposed on the surface; (ii) at Aismaola, a 3°-hinterlandward dip of all strata is assumed at the beginning of foreland deformation.

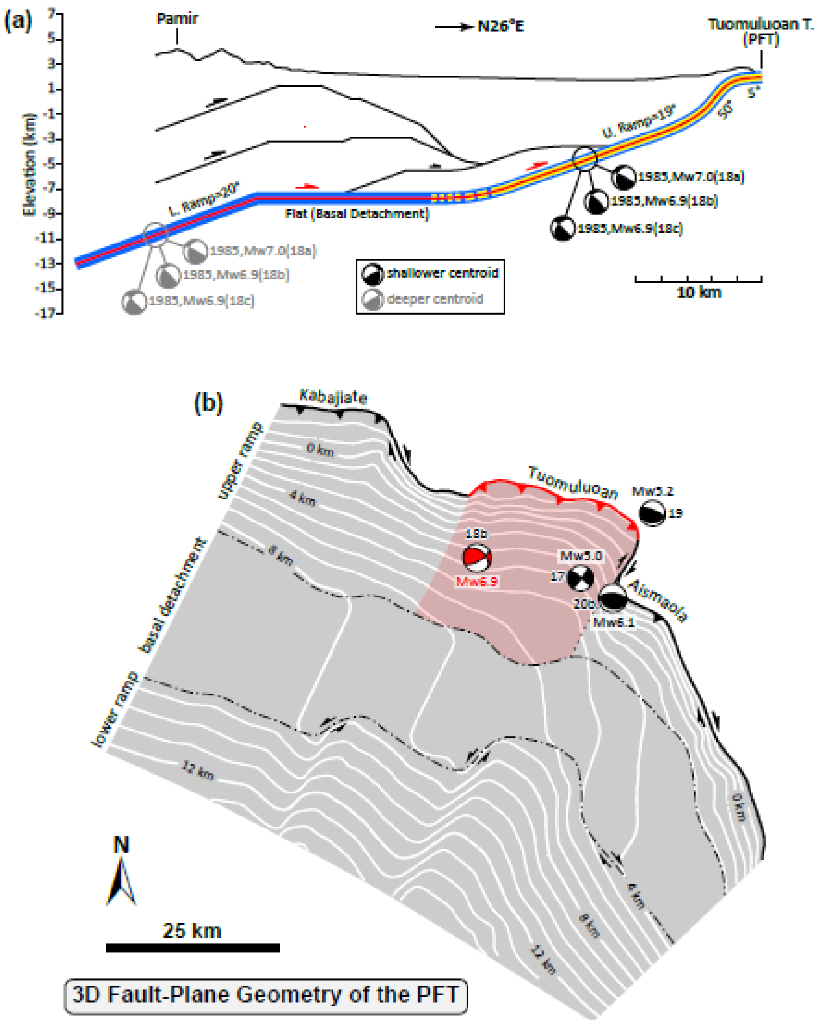

Figure 11. (a) Probable centroid locations and downdip rupture segments of the 1985 Wuqia earthquake. This event probably had either (i) a deeper centroid depth and totally ruptured the lower ramp, flat, and the upper ramp (bold blue line along the fault plane) or (ii) a shallower centroid depth and only ruptured the upper ramp (bold yellow line along the fault plane). (b) 3D fault-plane geometry of the Pamir Frontal Thrust interpreted from seismic reflection profiles, showing its along-strike and downdip segmentation characteristics. The geometric model is developed in the 2D MOVE software: the fault plane is interpreted on each seismic reflection profile, followed by mesh surface creation using the Delaunay-Triangulation method, after which the contours are created. Contours depicting depth below sea level. The interpreted base of the upper ramp and top of the lower ramp that bound the basal detachment are marked by two dashed lines. Prospective slip patch for the 1985 Wuqia earthquake is outlined in a red area. The numbers of seismic beach balls in Figures 11a, b and c correlate to those of analogous beach balls in Figures 2 and 3a.

Event	Date	Time, UT	Lat	Long	Magnitude	Strike	Dip	Rake	Strike	Dip	Rake	Depth	Reference[a]
1	Aug 22, 1902	-	39.86	75.62	M_w 7.7	80	60	90	260	30	90	18 km	3
2	May 11, 1967	14:51	39.33	73.74	M_w 5.8	317	88	-171	227	82	-2	8 km	2
3	Sept 14, 1969	16:15	39.7	74.8	M_w 5.8	279	44	104	79	47	76	3 km	2
4	Aug 11, 1974	01:13	39.51	73.78	M_w 7.0	283	51	126	53	51	53	2-5 km	2, 4
5	Aug 11, 1974	20:05	39.44	73.67	M_w 5.8	269	52	89	91	38	91	7 km	2
6	Aug 11, 1974	21:21	39.46	73.76	M_w 5.9	199	19	-155	86	82	-72	7 km	2
7	July 28, 1976	18:24	39.27	71.67	M_s 6.1	306	41	-38	66	67	-124	34 km	5
8	Oct 08, 1978	14:20	39.40	74.76	M_w 6.0	111	48	118	252	49	62	13 km	2
9	Nov 1, 1978	19:48	39.34	72.56	M_w 6.6	202	75	33	103	58	163	15 km	2
10	Nov 2, 1978	06:24	39.35	72.66	M_w 5.6	204	57	61	69	42	126	5 km	2
11	April 17, 1979	17:01	38.57	73.46	M_w 5.2	140	75	163	235	74	15	97 km	2
12	July 31, 1980	19:03	39.55	74.96	M_w 5.0	261	37	82	91	53	96	33 km	5
13	Feb 13, 1983	01:40	39.99	75.25	M_w 6.3	319	87	-178	228	88	-3	8 km	2
14	April 5, 1983	06:50	39.96	75.30	M_w 5.9	320	88	-176	229	86	-2	10 km	2
15	Dec 16, 1983	13:15	39.34	72.96	M_w 6.0	210	48	71	56	45	109	8 km	2
16	April 27, 1985	01:31	38.62	73.21	M_w 5.6	103	65	172	196	82	25	117 km	2
17	Aug 23, 1985	08:32	39.39	75.38	M_w 5.0	308	85	175	38	85	5	15 km	2
18a	Aug 23, 1985	12:41	39.43	75.22	M_w 7.0	315	29	159	63	80	62	15 km	5
18b	Aug 23, 1985	12:41	39.43	75.27	M_w 6.9	316	46	160	60	75	45	10-25 km	1
18c	Aug 23, 1985	12:41	39.49	75.27	M_w 6.9	298	44	132	66	59	56	16 km	2
19	Aug 29, 1985	23:39	39.47	75.49	M_w 5.2	294	66	103	85	27	63	15 km	2
20a	Sept 11 , 1985	20:45	39.36	75.41	M_w 6.1	299	50	110	90	44	68	10 km	5

20b	Sept 11 , 1985	20:45	39.36	75.44	M_w 5.9	271	60	81	108	31	104	7 km	1
20c	Sept 11 , 1985	20:45	39.36	75.44	M_w 6.0	271	54	73	118	39	111	6 km	2
21	April 30, 1987	05:17	39.75	74.6	M_w 5.7	298	46	93	113	44	86	15 km	2
22	June 8, 1987	13:30	39.73	74.62	M_w 5.2	297	27	90	117	63	90	15 km	2
23	Jan 6, 1988	15;31	39.63	75.53	M_w 5.3	246	29	67	92	63	102	37 km	2
24	Aug 12, 1988	18:58	39.64	74.53	M_w 5.5	293	34	82	122	56	95	15 km	2
25	Sept 23, 1988	04:46	39.6	74.56	M_w 5.1	313	69	100	106	23	64	15 km	2
26	March 29, 1990	16:19	39.42	73.26	M_w 5.4	276	56	178	7	88	34	22 km	2
27	April 17, 1990	01:59	39.38	75.03	M_w 6.0	217	67	23	118	68	156	15 km	2
28	Dec 25, 2002	12:57	38.95	74.90	M_w 5.7	71	79	56	325	36	160	15 km	5
29	Sept 1, 2003	23:16	38.71	75.32	M_w 5.7	358	71	-46	107	47	-153	15 km	5
30	April 10, 2008	07:17	39.48	75.05	M_w 5.0	302	45	119	84	52	64	13 km	5
31	Oct 5, 2008	15:53	39.53	73.82	M_w 6.6	236	36	62	89	59	109	3 km	4
32	Dec 08, 2010	08:21	39.41	72.77	M_w 5.5	87	87	163	178	73	3	21 km	5
33	Dec 07, 2015	10:04	38.65	73.2	M_w 5.4	294	56	177	26	88	34	20 km	5
34	June 26, 2016	11:17	39.47	73.43	M_w 6.4	249	62	94	61	28	83	17 km	5
35	Nov 25, 2016	14:24	39.27	74.14	M_w 6.6	110	78	-177	19	87	-12	19 km	5

[a] References are the following: 1-Burtman & Molnar (1993), 2-Fan et al. (1994), 3-Kulikova (2016), 4-Sippl et al. (2014), 5-Harvard centroid-moment tensor catalog

Table 1. Focal Mechanism Solutions of Earthquakes at the Pamir Front and Adjacent Areas

Table 2. A Summary of Determined Ramp Dip, Slip and Uplift of the PFT along profiles *A-G*.

Section	Lower Ramp Dip	Slip (km)						Total Uplift (km)
		F3	F2	F1	Lower Ramp	Total	Upper Ramp	
Section A	17°	12.5	10.0	9.5	20.5	43.0	≥22.0	12.5
Section B	20°	11.5	10.0	9.0	15.5	37.0	≥13.0	12.5
Section C	20°	8.5	10.0	7.5	14.5	33.0	≥18.5	11.0
Section D	18°	7.5	8.0	9.5	17.0	32.5	21-23	10.0
Section E	18°	8.0	7.0	7.5	6.5	29.0	≥17.0[a]	9.0
Section F	-	-	-	-	-	-	~14.0[a]	-
Section G	-	-	-	-	-	-	≥11.5	-

[a] Includes shortening of ~3.0 km of the Mushi anticline